Evaluating different methods for elevation calibration of MAX-DOAS instruments during the CINDI-2 campaign

Sebastian Donner[1], Jonas Kuhn[1,2], Michel Van Roozendael[3], Alkiviadis Bais[4], Steffen Beirle[1], Tim Bösch[5], Kristof Bognar[6], Ilya Bruchkouski[7], Ka Lok Chan[8], Theano Drosoglou[4], Caroline Fayt[3], Udo Frieß[2], François Hendrick[3], Christian Hermans[3], Junli Jin[9], Ang Li[10], Jianzhong Ma[11], Enno Peters[5,*], Gaia Pinardi[3], Andreas Richter[5], Stefan F. Schreier[12], André Seyler[5], Kimberly Strong[6], Jan-Lukas Tirpitz[2], Yang Wang[1], Pinhua Xie[10], Jin Xu[10], Xiaoyi Zhao[6,**], and Thomas Wagner[1]

[1]Max Planck Institute for Chemistry, Mainz, Germany
[2]Institute of Environmental Physics, University of Heidelberg, Heidelberg, Germany
[3]BIRA-IASB - Royal Belgian Institute for Space Aeronomy, Brussels, Belgium
[4]Laboratory of Atmospheric Physics, Aristotle University of Thessaloniki, Thessaloniki, Greece
[5]Institute of Environmental Physics, University of Bremen, Bremen, Germany
[6]Department of Physics, University of Toronto, Toronto, Canada
[7]National Ozone Monitoring Research and Education Center BSU, Minsk, Belarus
[8]Meteorological Insitute, Ludwig-Maximilians-Universität, Munich, Germany
[9]CMA Meteorological Observation Center, Beijing, China
[10]Anhui Institute of Optics and Fine Mechanics, Hefei, China
[11]Chinese Academy of Meteorological Sciences, Beijing, China
[12]Institute of Meteorology, University of Natural Resources and Life Sciences, Vienna, Austria
[*]now at: Institute for the Protection of Maritime Infrastructures, German Aerospace Center (DLR), Bremerhaven, Germany
[**]now at: Air Quality Research Division, Environment and Climate Change Canada, Toronto, Canada

Correspondence to: Sebastian Donner (sebastian.donner@mpic.de)

Abstract. We present different methods for in-field elevation calibration of MAX-DOAS (Multi AXis Differential Optical Absorption Spectroscopy) instruments that were applied and inter-compared during the second Cabauw Intercomparison campaign for Nitrogen Dioxide measuring Instruments (CINDI-2). One necessary prerequisite of consistent MAX-DOAS retrievals is a precise and accurate calibration of the elevation angles of the different measuring systems. Therefore, different methods

5 for this calibration were applied to 12 instruments from 11 groups during the campaign and the results were inter-compared.

This work first introduces and explains the different methods, namely far and near lamp measurements, white/bright stripe scans and horizon scans, using data and results for only one (mainly the MPIC) instrument. In the second part, the far lamp measurements and the horizon scans are examined for all participating groups. Here, the results for both methods are first inter-compared for the different instruments and secondly, the two methods are compared amongst each other.

10 All methods turned out to be well-suited for the calibration of the elevation angles of MAX-DOAS systems, with each of them having individual advantages and drawbacks. Considering the results of this study, the uncertainties of the methods can be estimated as ±0.05° for the far lamp measurements, ±0.1° to ±0.3° for the horizon scans, and around ±0.1° for the white stripe and near lamp measurements. When comparing the results of far lamp and horizon scan measurements, a spread of around 1° in the elevation calibrations is found between the participating instruments for both methods. This spread is on the order of

a typical field of view (FOV) of a MAX-DOAS instrument and therefore, affecting the retrieval results. Further, a consistent (wavelength dependent) offset of 0.31° and 0.40° between far lamp measurements and horizon scans is found, which can be explained by the fact that, despite the flat topography around the measurement site, obstacles such as trees might mark the visible horizon during daytime. The observed wavelength dependence can be explained by surface albedo effects. Lastly, the

5   results are discussed and recommendations for future campaigns are given.

1   Introduction

Multi AXis Differential Optical Absorption Spectroscopy (MAX-DOAS) is a well established method of ground-based remote sensing of trace gases and aerosols. MAX-DOAS instruments measure spectra of scattered sunlight at different (mostly low) elevation angles. Therefore, they have a high sensitivity to trace gases and aerosols located close to the surface (e.g., Hönninger

10   and Platt, 2002; Hönninger et al., 2004; Irie et al., 2008; Van Roozendael et al., 2004; Wagner et al., 2004, 2011; Wittrock et al., 2004). Such measurements allow the retrieval of vertical profiles of trace gases and aerosol extinction as well as column properties such as vertical column densities (VCDs) and aerosol optical depths (AODs) (e.g., Frieß et al., 2006; Irie et al., 2008; Clémer et al., 2010; Wagner et al., 2011).

     For the retrieval of these quantities, it is crucial to accurately know the measurement geometry, namely the solar zenith angle,

15   the relative solar azimuth angle and the telescope's elevation angle (Hönninger et al., 2004). While the solar zenith angle can be computed rather easily, it is more difficult to determine the relative solar azimuth angle and to calibrate the telescope's elevation angles. Although the relative azimuth has at least the same uncertainties as the elevation angle, it has a much weaker effect on the measurements (when assuming horizontal homogeneity of the trace gas distributions). An analysis of the CINDI-2 data set shows that for low elevation angles wrong pointing has a large impact on the retrieved trace gas differential slant

20   columns (dSCDs) which are the basic quantity obtained by MAX-DOAS (Hönninger et al., 2004). Panel (a) of Fig. 1 shows the mean dependence of the dSCDs on the elevation angle for the whole campaign and for different trace gases. Each curve was normalised to the mean dSCD of the respective elevation sequence. Panel (b) shows the relative changes in the retrieved trace gas dSCDs per degree pointing error for the same species. The curves were obtained by calculating the derivative of the dSCDs curves from panel (a) with respect to the elevation angle and dividing the results by the dSCDs at the corresponding

25   elevations. Although this approach remains qualitative, it shows clearly under which conditions pointing errors can lead to substantial biases in the dSCDs. As an example, an error of 1° in the telescope's elevation close to 0° elevation can lead to an error of around 20 % in the retrieved NO_2 dSCD, since the sensitivity of MAX-DOAS measurements depends strongly on the elevation angle and NO_2 is mainly located close to the surface.

     Since instruments and retrieval algorithms have improved significantly in recent years, uncertainties in the elevation cali-

30   bration now have a larger relative impact on the retrieval results and can become the dominating error source. Therefore, the calibration of the elevation angles of MAX-DOAS instruments has become an important topic for instrument operators (e.g., Roscoe et al., 2010; Piters et al., 2012). In the past, these calibrations were mainly done in laboratories where fixed target points were used as references and the elevations were calibrated accordingly. However, when the instruments were brought

to the field, only rarely (if at all) the accuracy of the a-priori elevation angle calibration was checked under real measurement conditions.

In this work, different methods for in-field elevation calibration of MAX-DOAS instruments, which were applied by numerous groups during the CINDI-2 campaign, are presented, evaluated and compared amongst each other. Furthermore, recom-
5 mendations for the setup of MAX-DOAS measurements are derived based on the results of the comparison.

The paper is structured as follows. First, a short overview of the CINDI-2 campaign and the participating instruments is given in Sect. 2. Section 3 introduces and examines the different methods of elevation calibration for one (mainly the instrument of the Max Planck Institute for Chemistry (MPIC)) instrument and a first comparison between the different methods is given. Comparisons between the participating instruments for the different methods are presented in Sect. 4. Additionally,
10 the methods are compared amongst each other in detail. A final discussion is presented in Sect. 5, together with conclusions and recommendations for upcoming MAX-DOAS measurements.

2 Campaign overview and MAX-DOAS instruments

In this section, an overview of the CINDI-2 campaign (Sect. 2.1) and the MAX-DOAS instruments (Sect. 2.2) which participated in this study is given.

2.1 The CINDI-2 campaign

The second Cabauw Intercomparison campaign for Nitrogen Dioxide measuring Instruments (CINDI-2) took place in September 2016 at the Cabauw Experimental Site for Atmospheric Research (CESAR) in the Netherlands. It was a follow up to the CINDI campaign, which took place at the same site in June 2009 (Roscoe et al., 2010; Piters et al., 2012; Pinardi et al., 2013; Frieß et al., 2016). The main objective of the CINDI-2 campaign was the inter-comparison of different ground-based
20 remote sensing - mostly MAX-DOAS - instruments, including several calibration exercises to harmonise the measurements of the different instruments. For the interpretation of the trace gas (e.g. NO_2) inter-comparisons, an accurate and consistent elevation calibration is essential. Therefore, an elevation calibration exercise was included in the campaign plan. More detailed descriptions of the CINDI-2 campaign and its objectives are given in Kreher et al. (2019) and Apituley et al. (2019).

Many instruments which were operated during the campaign also participated in different elevation calibration exercises that
25 were conducted throughout CINDI-2 and are summarised in this work. In the following subsection, some technical details of the different instruments are presented.

2.2 Participating MAX-DOAS instruments

In total, 12 instruments from 11 groups with rather different measurement setups participated in the elevation calibration exercises. Table 1 gives an overview on the participating groups and defines instrument acronyms and instrument IDs. The
30 key properties of the participating instruments which are of relevance for this study are summarised in Table 2. Both tables are based on the CINDI-2 planning document (http://www.tropomi.eu/data-products/planning-information, last accessed on

17th March 2019) and information given in Kreher et al. (2019), where additional details on the instruments are provided. Table 2 indicates the variety and different properties of the participating instruments.

3 Methods of elevation calibration

This section introduces the different methods for the calibration of the elevation angles of MAX-DOAS instruments that
5 were applied by at least one group during the CINDI-2 campaign. First, the common general approach which is underlying all methods is explained (see subsection 3.1), followed by detailed descriptions and evaluations of the individual methods (subsections 3.2 to 3.5). Subsection 3.6 gives a consistency check between the different methods using data of the MPIC instrument.

3.1 General approach

10 As already mentioned, MAX-DOAS instruments which are brought to field campaigns typically have an a-priori calibration of the elevation angles which was obtained in the laboratory. However, for high quality measurements this a-priori calibration has to be checked and (if needed) to be adjusted in field. Therefore, four different methods for the in-field calibration of the elevation angles of MAX-DOAS systems are described and evaluated in the following sections. All of them use the same basic principle which is described in this section.

15 First, a specific target is placed in front of the optical unit of a MAX-DOAS instrument (see Fig. 2). The elevation angle β of this target relative to the horizontal line of the telescope unit has to be determined very accurately in order to use this elevation as a reference. Next, an elevation scan across the target is performed and the apparent elevation angle $\widehat{\alpha}$ of the target is retrieved using the measured intensities at different elevation angles α_i. Here, α_i denotes elevation angles measured relative to the a-priori elevation calibration of the instrument. In that way, an elevation offset $\gamma = \beta - \widehat{\alpha}$ can be calculated and used to
20 correct the elevation angles measured relative to the a-priori elevation calibration of the instrument ($\alpha' = \alpha + \gamma$). Further, this offset γ can be used to adjust the a-priori elevation calibration of the MAX-DOAS system by shifting the a-priori horizontal line by $-\gamma$. However, it should be noted that this principle used by all the different methods described in this work only calibrates one specific elevation angle, usually 0°. Thus, the accuracy of the other elevations depends on the internal accuracy of the motor and its steering unit. Many instruments (e.g. the CMA MiniDOAS instrument and the MPIC Tube MAX-DOAS
25 instrument) approach the other elevation angles by moving the telescope by a defined number of motor steps (per degree) relative to the motor position that corresponds to the horizontal line of the telescope (0° elevation). Others however (e.g. the 2D-EnviMes instruments), use an inclinometer inside the telescope unit which also enables these instruments to actively correct their elevation angles for possible deviations. Many other methods to deal with this internal elevation calibration are possible, but this topic is not discussed in more detail in this paper. Further, it should be mentioned that the elevation calibration might
30 be different for different azimuthal directions which is important for 2D instruments.

A sketch of the general measurement setup can be found in Fig. 2, further, a graphic definition of all relevant angles is provided in this figure. In the following sections this principle is applied to different target types and the results are evaluated.

3.2   Far lamp measurements

3.2.1   Approach

For the first method, an artificial light source is used as target that is located at a far distance (around 1 to 2 km) from the instrument's telescope and typically close to the visible horizon. Since this method uses an artificial light source, the elevation
5   scan across this target has to be done during nighttime.

During the CINDI-2 campaign, a xenon lamp was used as light source and was placed at around 1280 m distance from the measurement site in the main viewing direction of the MAX-DOAS instruments at an azimuth angle of 287° (compare upper part of Fig. 3). The light of the lamp was directed towards the instruments using a large aperture lens with a diameter of 17 cm. Using the connected water channels located next to both the measurement site and the lamp site, we could determine and mark
10   the vertical position of the lamp at the measurement site (see lamp mark in the lower part of Fig. 3). In that way, the expected elevation angle β of the lamp relative to the horizontal lines of the optical units of the individual MAX-DOAS systems could be inferred. The layout of the measurement conditions and the measurement setup geometry are summarised in Fig. 3.

Such xenon lamp measurements were done on several days (8th, 10th, 13th and 19th September) throughout the campaign, although not all instruments participated on all nights. In the next section, the analysis of the lamp measurements is explained
15   in more detail using data from the MPIC instrument.

3.2.2   Results for the MPIC instrument

Data from the far lamp measurements are available for four nights for the MPIC instrument. On all of these nights, a fixed elevation calibration was used and the scan resolution was 0.02° (except on 8[th]September, when the scan resolution was 0.1°; compare last column of Table 3). The initial elevation calibration was obtained by using lamp measurements from an
20   earlier night, when the lamp measurements were tested. In the following, the analysis is done for three wavelengths, which are distributed over the detector range of the instrument and correspond to strong emission lines of the xenon lamp. An example spectrum of the xenon lamp which was measured on 13th September is shown in Fig. 4. The three distinct emission lines at 365.16 nm, 404.90 nm and 435.96 nm that were used for the analysis are clearly visible.

As first step of the analysis, the measured intensities are normalised with respect to their total integration time and linearly
25   interpolated between the two detector pixels closest to each of the three selected wavelengths. These intensities are then plotted against the elevation angle for the different scans. As an example, the intensity curve at 435.96 nm obtained for 13th September is shown in Fig. 5. The curve obviously shows a minimum where a maximum would be expected if we assume a Gaussian-shaped curve. However, we can understand this feature when we take into consideration that in the focal point of the telescope, a quartz glass fibre bundle is mounted as illustrated in Fig. 6. First, we calculate the size of the image of the xenon lamp inside
30   the instrument's telescope (yellow spot in Fig. 6). Given the geometry of the measurement setup, namely the diameter of the xenon lamp and the dimensions of the telescope, this leads to an image size of around 7 µm at the entrance of the fibre bundle. Taking into account that the glass fibre bundle consists of four individual fibres with a light-conducting diameter of 200 µm each, the obtained image size is only 3.5 % of a single fibre diameter. In that way, it is possible that the image of the lamp hits

the space between the individual fibres when performing an elevation scan (dashed line in Fig. 6 indicates the idealised scan axis) and therefore an intensity minimum is found when exactly pointing at the light source. These calculations were done assuming idealised conditions (fibre exactly located in the focus, no aberration of the lens etc.) and the resulting image of the xenon lamp would lead to a much more pronounced and wider minimum than the one in Fig. 5. However, in reality the lens

5   has an aberration and the fibre bundle might be located not exactly in the focus of the lens, further, the scan axis might not pass through the center of the fibre bundle. These effects lead to a less symmetric intensity distribution which does not reach zero intensity at its center (compare Fig. 5).

In order to determine the elevation angle $\widehat{\alpha}$ under which the xenon lamp could be seen, the center of the intensity curve (see dashed red line in Fig. 5) is calculated using the center of mass formula:

$$\widehat{\alpha} = \frac{\sum s_i \cdot \alpha_i}{\sum s_i}, \tag{1}$$

where s_i denotes the intensity measured at the elevation angle α_i. Using this equation yields a lamp elevation of $0.02°$ for the intensity curve shown in Fig. 5. Here, it should be noted that Fig. 5 shows the intensity curve of an elevation scan that was performed by approaching the elevation angles from below. For scans where the angles were approached from above, the centers are found consistently at lower elevations by around $0.4°$. Because of that, we assured that all elevation angles were

15   approached from below for the other calibration exercises and the regular measurement protocol.

Equation (1) is used to calculate the centres of the intensity curves for all three wavelengths and all four days. The corresponding lamp positions are summarised in Table 3. Taking into account that the minimum motor step size is $0.01°$, the different values are consistent with each other within the span from $-0.01°$ to $0.02°$ (excluding 8th September, when the scan resolution was only $0.1°$). Here, it should be noted that the center of a Gaussian fit (see red fit curve in Fig. 5) yields consistent

20   lamp elevations compared to the center of mass approach which was applied here. Therefore, also for the MPIC instrument, a Gaussian fit is used in Sect. 4.1, where the lamp scans of all instruments are analysed in a consistent way.

As already mentioned above, the position of the artificial light source relative to the instrument has to be known very accurately in order to calibrate the elevation angles of the MAX-DOAS system. Based on the setup summarised in Fig. 3, an expected lamp elevation of around $-0.04°$ is obtained, when using an estimated height difference, Δh, of $1\,\mathrm{m}$ between the

25   xenon lamp and the telescope unit. It should be noted that the Earth's curvature at a distance of $1280\,\mathrm{m}$ corresponds already to $-0.011°$ and is therefore not negligible. Adding this offset to the obtained lamp elevation, the MPIC MAX-DOAS system should find the lamp at around $-0.05°$ elevation. If we compare this value to the values given in Table 3, we can conclude that the instrument sees the lamp close to the expected position. The small deviations between the table values and the expected elevation can be explained by a combination of several small uncertainties, namely, the minimum motor step size of $0.01°$, the

30   used scan resolution of $0.02°$ and the uncertainties of the calculation of the lamp position $\widehat{\alpha}$ using Eq. (1).

The relatively small span of lamp positions obtained on different days and at multiple wavelengths indicates that this method is very stable and reproducible. Furthermore, this approach allows the calibration of several instruments with the same setup at the same time, since all instruments can point at the same target. However, depending on the slight horizontal distances of the

different measurement locations, small differences in the azimuth angle (up to 1.8° for the CINDI-2 campaign) under which the lamp can be seen have to be taken into account. A drawback of this method is that the position of the artificial light source relative to the instrument has to be determined accurately, which might be challenging or even impossible at some locations. Also finding a suitable location for the lamp can be difficult e.g. in cities.

3.3 Near lamp measurements

3.3.1 Approach

This method also uses an artificial light source during nighttime, but here it is located rather close to the instrument's telescope (a few meters). In order to determine the expected lamp position, namely $\beta = 0°$, the light source has to be aligned to the (center of the) telescope unit of the instrument. This alignment is typically done using a laser level. Both the setup and the alignment procedure are sketched in Fig. 7. Using this procedure, the light source should be found at 0° elevation and possible deviations from that position can be used to correct the elevation calibration.

Such near lamp measurements were not performed for the MPIC instrument during the CINDI-2 campaign. However, the elevation angles of the IUP-HD instrument were calibrated using this method. Therefore, in the following, data from the IUP-HD instrument are used to illustrate this method and its analysis in more detail.

3.3.2 Results for the IUP-HD instrument

Three such near lamp scans were done by the IUP-HD group in one night in the preparation phase of the CINDI-2 campaign. Mean intensities are calculated separately for the UV and VIS spectrometer. It should be noted that the first two scans were performed in an elevation range from −2° to 2°, while the last was done in a range from −1° to 0.45°. In order to analyse these measurements, the (normalised) mean intensities are plotted against the elevation angle α reported by the measuring system. Next, a Gaussian function of the form

$$S(\alpha) = A + B \cdot \exp\left(-\frac{(\alpha - \widehat{\alpha})^2}{2 \cdot \sigma^2}\right) \tag{2}$$

is fitted to the intensities and the center $\widehat{\alpha}$ of this function represents the lamp elevation. Further, $S(\alpha)$ represents the fitted intensity at a given elevation, A represents an intensity offset, while B describes the maximum of the fitted curve. The width of the fitted curve is controlled by the parameter σ. For improving the statistics, all three scans are plotted in one plot (using different colours for the individual scans) and the Gaussian fit is applied to the whole data set of one spectrometer (see Fig. 8).

The retrieved lamp elevation is also shown in this figure. Following this procedure, lamp elevations $\widehat{\alpha}$ of −0.14° and −0.11° were found in the UV and visible spectral range, respectively. These lamp elevations can be now used to adjust the initial elevation calibration of the instrument.

3.4 Horizon scans

3.4.1 Approach

A common method for the calibration of the elevation angles of MAX-DOAS systems is the so-called horizon scan. Here, the elevation β of the visible horizon is used as reference. Since this method does not require an active light source, it can

5   be performed during daytime and the variation in the measured intensity at the horizon is used to determine its position. A Gaussian integral is fitted to the measured intensities and the fit parameters give the horizon position. In practice, sometimes the numerical derivative of the intensity curve is calculated since below the horizon the intensity does not approach zero but the rapid change of the measured intensity allows the identification of the horizon position $\widehat{\alpha}$. A further prerequisite of this method (despite the knowledge of the expected elevation of the visible horizon) is that the horizon has to show a clear and rapid change

10   in intensity, which might not be fulfilled during episodes of fog or very low clouds, when the horizon might be blurred. In that case no clear conclusions can be drawn from horizon scans. Furthermore, it should be noted that the visible horizon should not be too far away (less than a few kilometers) to minimise the influence of atmospheric scattering.

During the CINDI-2 campaign, horizon scans were included in the measurement protocol in order to study the consistency and stability of the elevation calibration of the different measurement systems. Thus, all MAX-DOAS instruments (both 1D

15   and 2D) performed horizon scans between 11:40 UTC and 11:45 UTC at a specified total integration time of 5 s while pointing in the main viewing direction (287° azimuth angle). The scans were done using predefined elevation angles between −5° and 5°, whereby the scan resolution was 0.2° in the interval between −2° and 2° and 1° outside this range.

3.4.2 Results for the MPIC instrument

For the MPIC instrument, horizon scan data is available starting from 17th September until 2nd October. Before 17th September

20   some horizon scans were performed as well, but they are of limited quality due to an error in the measurement script of the MPIC system. Furthermore, some days are not used either due to bad weather conditions with fog and many low clouds or due to known pointing problems. On overall 10 days, useful horizon scan data are available for the MPIC instrument.

First, the measured intensity is normalised with respect to the total integration time. As a second step, the intensity curves are also normalised to their corresponding maximum allowing a direct comparison of the intensity curves recorded on different

25   days with various sky conditions. The normalised intensity curves obtained at 340 nm for the different days are shown in Fig. 9(a) (coloured dots). Here, the increase of the measured intensity around the horizon is clearly visible in an elevation range from around 0° to 1°. Next, a Gaussian integral of the form

$$S(\alpha) = A \cdot \left(\mathrm{erf} \left(\frac{\alpha - \widehat{\alpha}}{B} \right) + 1 \right) + C \cdot (\alpha - \widehat{\alpha}) + D \qquad (3)$$

is fitted to the data since this approach is more stable than calculating a numerical derivative. Here, S represents the fitted

30   intensity, α the elevation angle and the parameters A, B, C and D determine the exact form of the fitted curve. The parameter $\widehat{\alpha}$

indicates the center of the fitted function and therefore represents the derived horizon elevation. The resulting daily fit functions are also displayed in Fig. 9(a) by lines in the corresponding colours.

Additionally, the analytical derivative of Eq. (3) can be calculated. The resulting curves (see Fig. 9(b)) contain information on the instrument's field of view (FOV) since the full width at half maximum (FWHM), which is a typical measure for the

5   FOV, can be derived:

$$FWHM = 2\sqrt{\ln 2}B. \tag{4}$$

By following this procedure, a value of 0.30° is found as the median center (vertical red line in Fig. 9) for the fitted functions representing the median horizon elevation for the MPIC instrument at 340 nm. However, it should be mentioned that there is quite some scatter in the daily horizon scans, which might be caused by varying sky conditions on the different days and is

10   one of the drawbacks of this method. The same procedure is also applied to the intensities recorded at 440 nm in order to study possible wavelength dependencies, the resulting intensity curves and derivatives are shown in Fig. 9(c) and (d). Here, a median horizon elevation of 0.37° is obtained, which is slightly higher than the value for 340 nm. These two wavelengths were chosen for the analysis because they were reported by all instruments that participated in the semi-blind inter-comparison during the campaign and thus, they are well suited for a comparison of the horizon scan results for different instruments (see Sect. 4.2).

15   ## 3.5   Bright/white stripe scans

3.5.1   Approach

The white stripe method can also be applied under daylight conditions and a white or at least bright stripe in front of a black/dark background is used as reference target. In order to calibrate the elevation angles, the (center of the) white stripe has to be aligned with the (center of the) telescope, archiving an expected stripe position of $\beta = 0°$. This can be done by using a

20   water or laser level.

The setup applied by MPIC during the CINDI-2 campaign used an adjustable white stripe in front of a dark plate and a large water level which consisted of two bottles of water which were connected via a 10 m long tube filled with water and positioned next to the stripe and the telescope. On the telescope side the water level has to be adjusted to the middle of the telescope, thus on the plate stripe side the water level indicates the altitude of the telescope. Here, the stripe has to be adjusted to the water level

25   position which guarantees the alignment of stripe and telescope axis. A sketch of the described setup can be found in Fig. 10. The horizontal distance between the telescope and the white stripe was 342 cm and the vertical extension of the stripe was around 2.5 cm which corresponds to a FOV of around 0.4°. This apparent FOV is quite large and shows that the setup was not optimised but the rather short distance between telescope and stripe was determined by the local conditions (a water channel in front of the instrument container limited the maximum distance which could be achieved). Therefore, this calibration method

30   using the here described setup was applied only once during the campaign and only for the MPIC instrument. However, other groups (e.g. BIRA) applied the same method using their own setups. The scan resolution was 0.05° which was a compromise

between speed (needed because of the unstable setup) and accuracy. In the following, the analysis is done for two wavelengths, namely 340 nm and 440 nm in order to be consistent with the approach described in Sect. 3.4.

3.5.2 Results for the MPIC instrument

Again, the recorded intensities are first normalised with respect to their total integration time. Next, a background correction is
5 applied to the intensity curves, which is needed since the dark background of the white stripe does not absorb all incident light. For that, a second order polynomial is fitted to the background intensities and subtracted from the measured intensities. The resulting intensity curve at 440 nm and the fitted Gaussian function (compare Eq. (2)) are depicted in Fig. 11. Now, the center $\widehat{\alpha}$ of the Gaussian fit indicates the stripe position. In that way, a value of −0.01° is found (red dashed line). Since the intensity curve again shows no smooth behavior (see Sect. 3.2), additionally the center of mass approach following Eq. (1) is applied,
10 yielding a stripe position of −0.02° (blue dashed line) consistent with the Gaussian approach. Conducting the same procedure for the intensities measured at 340 nm yields values of 0.02° and 0.00° for the Gaussian and center of mass approaches, respectively.

In summary, a range of −0.02° to 0.02° for the retrieved stripe positions is obtained, which corresponds to only four motor steps. Similarly to the far lamp measurements (Sect. 3.2) this range can be explained by the minimum motor step size of 0.01°,
15 the used scan resolution of 0.05° and the uncertainties of the retrieval of the stripe position $\widehat{\alpha}$. Further, also the angular height (0.4°) of the white stripe was quite large.

3.6 Comparison between the different methods

In this section, the different methods for the elevation calibration of MAX-DOAS instruments are compared and examined with respect to their consistency. Table 4 summarises the retrieved target elevations $\widehat{\alpha}$ using the methods introduced above (except
20 the near lamp measurements which were not done for the MPIC instrument).

A comparison of the results for the far lamp measurements and the white stripe scans shows very good agreement, with small deviations that can be explained by the already mentioned motor step size of 0.01° and the different scan resolutions. For both methods, no significant wavelength dependence of the retrieved horizon positions is visible.

However, comparing the results for these two consistent methods to the results of the horizon scans shows larger deviations.
25 The retrieved median horizon positions from the horizon scans for 340 nm and 440 nm were 0.30° and 0.37°, respectively, which are significantly higher than the values around 0° found with the other two methods. During the campaign, the xenon lamp was placed close to the visible horizon but at ground level as already explained in Sect. 3.2. However, during the day the visible horizon is not represented by the ground but by a row of trees situated close to the lamp location in the main viewing direction of the MAX-DOAS instruments. Thus, the visible horizon would correspond to around 6.5 m to 8.0 m height above
30 the altitude of the lamp which explains the deviations (of about 0.3° to 0.37°) to the other two methods. A further effect which can be observed for the horizon scans is that the median horizon elevation is significantly lower for 340 nm compared to the one obtained at 440 nm. As we will see in the next section, this effect is also found for the other participating MAX-DOAS

systems. Besides this systematic wavelength dependency of the horizon scans, the results of the different methods agree quite well amongst each other when taking the uncertainties into account.

4   Comparison between different instruments

In this section the results of the far lamp measurements and the horizon scans are inter-compared between the different participating groups.

4.1   Comparison of the far lamp measurements

Far lamp measurements using the xenon lamp as described in Sect. 3.2 were performed in several nights throughout the campaign. However, not all instruments participated each time. Since the different instruments use rather different instrumental setups and scanning schemes, they are divided into three groups.

The first group consists of 2D instruments which performed full 2D scans of the xenon lamp in vertical (elevation angle) and horizontal (azimuth angle) direction on at least one night. For these instruments, the measured intensities are first normalised with respect to integration time and interpolated to specific wavelengths in order to compare the results of the different methods and instruments. Panels (a) of Fig. 12 to 15 show representative examples of the obtained 2D intensity distributions for the BIRA (Fig. 12), IUP-HD (Fig. 13), UToronto (Fig. 14) and LMU instrument (Fig. 15; for this instrument only the mean intensities of the spectra are available), respectively. Additionally, black dotted lines indicating the azimuth angle under which the maximum intensity was recorded can be found in these figures. The axes of these figures were chosen in a way that they all show the same relative elevation (1°) and azimuth span (1.2°). While the BIRA instrument shows a very smooth and smeared out distribution of the measured intensities, the intensity distributions are more sharp for the UToronto (still quite smooth), IUP-HD, and LMU instruments. This finding can be explained by the different FOVs of the instruments and their different fibre configurations which are used to transmit the collected light to their detectors. As shown in Table 2, the FOV of the BIRA UV instrument is 1°, while they are smaller for the other three instruments, namely 0.4°, ca. 0.4° and ca. 0.6° for the LMU, the IUP-HD and the UToronto instruments, respectively. This larger FOV leads to a smearing out of the measured intensity distribution of the BIRA UV instrument. Further, the fibre configuration inside the telescope units of the four instruments has an influence on the actual shape of the measured intensity distributions. While the LMU and IUP-HD instruments used a ring of fibres inside their telescope units (for the UV channel), the UToronto and the BIRA UV instruments used a spot configuration, consisting of 37 and 51 fibres, respectively, inside the telescope. When scanning across the xenon lamp, it might occur that the FOV is not always fully illuminated at the "edges" of the xenon lamp light beam. The ring configuration might be more sensitive (similarly to the fibre effect found for the MPIC instrument in Sect. 3.2) to this effect and introduce more edges to the measured 2D intensity distributions, leading to a sharper shape.

Two approaches were applied to retrieve the horizontal position under which the lamp is found for this first group of instruments. For the first approach, the intensities along a transect (black dotted lines in panels (a)) are extracted and a Gaussian function is fitted to these intensities (compare Eq. (2)). The centers $\widehat{\alpha}$ of these fits represent the lamp elevations, the intensity

curves and Gaussian fits for the four examples can be found in panels (b) of the respective figures. For the second approach, all intensities which were recorded at one specific elevation angle are integrated over the different azimuth angles. These values are then used for the analysis and again, the center of a Gaussian fit indicates the vertical position of the light source. Panels (c) of Fig. 12 to 15 depict the resulting curves and fits for the four instruments. The results of the two methods are very consistent

5 for a single instrument. Nevertheless, there is quite some spread between the different instruments, which will be investigated in more detail at the end of this section.

The second group are 2D instruments which performed cross-scans, meaning that first an azimuth scan was performed, followed by an elevation scan at the azimuth direction under which the maximum intensity was found. This was done by three instruments using individual scanning schemes. Examples of the obtained intensity curves and corresponding Gaussian fits are

10 depicted in Figure 16. The different panels of this figure show the curves, fits and resulting centers for the AUTH (a), BOKU (b) and IUB-B (c) instruments, respectively. The results for the lamp position are rather consistent for the different scans for an individual instrument since the obtained centers are nearly the same. This is also valid when looking at the results for different wavelengths for one instrument (not shown here). However, it can be seen that there is some spread between the different instruments.

15 The last group consists of 1D instruments which performed simple elevation scans of the xenon lamp as described in Sect. 3.2. For these instruments, the normalised intensity is plotted against the elevation angle and the center of a Gaussian fit gives the lamp elevation. Examples for the CMA UV, CMA VIS, BSU and AIOFM instruments are shown in Fig. 17, with the resulting lamp elevations (centers) also displayed. Since the BSU instrument has a 2D CCD on which the second dimension represents the elevation angle, it should be noted that this instrument did not really scan across the lamp but each image on the

20 CCD represents a full lamp scan. The AIOFM instrument is a 2D instrument, but was operated in 1D mode for the far lamp measurements.

For each participating instrument, the intensity curves are extracted for all valid lamp measurements by applying the respective procedure explained above for different wavelengths (365 nm, 405 nm, 436 nm and 546 nm) corresponding to the individual spectral ranges of the instruments. Further, a Gaussian function (compare Eq. (2)) is fitted to the data. The fit param-

25 eters are initialised by $A_0 = 0$, $B_0 =$ maximum of the measured intensity curve, $\widehat{\alpha}_0 =$ center of mass (calculated using Eq. (1)) and $\sigma_0 = 0.5°$.

The resulting lamp elevations are summarised in Fig. 18, where the mean of all retrieved lamp elevations (at different wavelengths and/or scans/days) for each instrument is shown as dots. Further, for each instrument, three different measures for the uncertainties of the retrieved lamp elevations are displayed. The left error bar of each instrument indicates the mean of all

30 fit errors of the fits explained above and measures the quality of the individual fits and the shape of the measured curves. The error of the mean of all retrieved lamp elevations is represented by the middle error bar. It is a measure of the consistency and stability of the results of the different lamp scans performed by one instrument. However, this quantity also depends on the actual number of available intensity curves at different wavelengths and days which is given in brackets behind the institute acronyms on the x-axis in Fig. 18. Lastly, the right error bar indicates the daily spread which is only available for instruments

35 which performed more than one scan on one day and for all 2D instruments, since two methods were applied to extract the 1D

intensity curves. The daily spread of one day is defined as the standard deviation of the results of the different scans on that day. If in addition several days are available, the mean of the daily standard deviations is calculated and displayed.

As shown in Fig. 18, a rather high spread of around 0.9° is found for the retrieved lamp elevations. Nevertheless, the values are centered around the expected values of −0.19° (dashed blue line) and −0.05° (dashed green line) for the instruments located

5 on the upper (mostly 2D instruments) and lower (mostly 1D instruments) row of containers installed at Cabauw, respectively. These slightly different values are due to the geometry of the measurement setup (compare Sect. 3.2 and Fig. 3) and are in agreement with the fact that the instruments on the second row of containers are located around 3 m higher than the instruments on the lower row for which a Δh of 1 m is assumed as in Sect. 3.2. Also most of the error bars for the individual instruments are quite small, indicating the good stability and high accuracy of the far lamp measurements. The large error bar for the mean

10 fit error for the LMU instrument can be explained by a rather uneven intensity distribution which leads to bad fit results in some cases.

The deviations between the different instruments are on the one hand caused by slightly different vertical positions (even if they are located on the same container level) of the instruments, since some of the instruments were mounted on tripods or similar devices while other instruments were placed closer to the container roof. On the other hand, the deviations are also

15 caused by the fact that all groups reported their elevation angles corresponding to their own elevation calibrations. Therefore, the spread of about 0.9° of the retrieved lamp elevations (for one container level) is a measure of the consistency between the elevation calibration of the different instruments.

More details will be discussed in Sect. 4.3, where the derived lamp elevations are compared to the corresponding horizon elevations obtained from the daily horizon scans which are inter-compared in the next section.

20 ## 4.2 Comparison of the horizon scans

As mentioned above, during the day the visible horizon might be defined by obstacles such as trees. The horizon elevations of the MPIC instrument were used to estimate the height of the visible horizon above the lamp altitude yielding values of 6.5 m and 8 m at 340 nm and 440 nm, respectively. Taking into account the expected lamp elevations (see Sect. 4.1), we estimate the elevation of the effective horizon to be 0.24° at 340 nm and 0.31° at 440 nm for the instruments on the lower row of containers.

25 However, since some of the other instruments (mainly the 2D ones) were located on the second row of containers, which was around 3 m above the lower row, the expected horizon elevation for these instruments is lower and we derive elevations of 0.10° and 0.17° if we use the same assumptions. As we will see below, the difference between the estimated horizon elevations for the two rows is smaller than the spread of the results of the horizon scans between the individual instruments.

In the following we use the results of the horizon scans of the participating instruments derived from the reported intensities

30 of the daily horizon scans at 340 nm and 440 nm following the approach explained in Sect. 3.4 and Kreher et al. (2019).

First, median horizon elevations are calculated for both wavelengths for all instruments. These median values (dots) are depicted in Fig. 19 together with the corresponding 25 % and 75 % percentiles (lines) which are a measure of the spread of the daily horizon elevations. No percentiles are shown for the NIWA_30 instrument since horizon scans were reported only for one single day. The values at 340 nm are represented by blue dots and lines, while red dots and lines indicate the values at

440 nm. Additionally, the expected horizon elevations at 340 nm and 440 nm for the instruments on the upper container row are displayed as blue and red dotted lines, respectively. It should be mentioned that only results for instruments which reported valid horizon scans on at least one day are shown.

Obviously, the retrieved horizon elevations have a quite large scatter of around 0.9° which is on the order of a typical FOV of a MAX-DOAS system. This finding is consistent with the spread of the lamp elevations that were discussed in the previous section. Nevertheless, the results for many instruments are centered around the estimated values from above. Especially, the results of the Pandora systems (operated by LuftBlick and NASA) which use the sun to calibrate the elevation angles are very close to that value. As indicated previously, the calculated difference of around 0.14° between upper and lower row in the elevation of the visible horizon is insignificant compared to the rather large scatter between the individual instruments. Even calculating mean or median horizon elevations for the instruments located on the upper and lower row does not reveal this expected difference (compare Table 5). However, when excluding some obvious outliers in the calculation of the mean (or median) elevations, there is some indication of this effect which this would be, however, rather arbitrary.

Looking at the percentiles of the individual instruments shows that for many of them the results of the daily horizon scans have a high degree of consistency which is indicated by the rather small percentile lines in Fig. 19. However, some instruments (e.g. the CMA instruments, the AUTH_3 or the LMUMIM_35 instruments) show quite large percentile lines, indicating more variable results of the daily horizon scans. This finding can also be seen in Fig. 20 and 21, where the results of the horizon scans at 340 nm and 440 nm are displayed on a daily basis for the individual instruments (blue dots), together with the corresponding median horizon elevations (blue dashed lines). The instruments having small percentile lines show a smooth behaviour in the daily horizon elevations, while the ones having larger percentile lines show a higher dispersion (e.g. the CMA_7 instrument). Some of the instruments (e.g. the LMUMIM_35 instrument) show a systematic behaviour in the daily results which might indicate adjustments of the elevation calibrations of these instruments, especially in the beginning of the campaign.

The rather large scatter between the instruments has several reasons. First, the individual instruments are placed at slightly different heights due to their specific instrumental setup even if they are located on the same container level. Further, the horizon is not a smooth line and the exact horizon position depends on the exact azimuth pointing direction and the actual shape of the horizontal line. Also a limited accuracy of the initial elevation calibrations of some instruments might contribute to this rather high dispersion of the horizon elevations. Lastly, also the weather (especially clouds) and visibility have a significant influence on the results of the horizon scans since they have an impact on the actual intensity variation around the visible horizon.

Another finding is that the horizon at 340 nm is found at significantly lower elevations compared to 440 nm for all instruments which reported both intensities. However, it should be mentioned that for some instruments (e.g. the BIRA instrument), the different wavelength ranges are recorded using separated sensors and even separate optical entrance systems. Nevertheless, these instruments show the same systematic difference. This finding is consistent with the results obtained with the MPIC instrument but so far no completely clear explanation could be found. However, an investigation of the intensity curves at different wavelengths for the horizon scan performed on one day shows an unexpected intensity variation at 0° elevation. An example is shown in panel (a) of Fig. 22 which displays the normalised intensity curves at different wavelengths measured on 17th September (similar behaviours are found on other days). Here, a local minimum is visible at 0° elevation for wavelengths

above 370 nm, which gets more pronounced for increasing wavelengths. This minimum influences the Gaussian integral fits (dashed lines in 22(a)) and the retrieved horizon elevations $\widehat{\alpha}$ show a quite smooth wavelength dependence as depicted in panel (b) of Fig. 22. These findings indicate a surface albedo effect. Pictures from the site show that in the visible spectral range the trees close to the horizon appear darker than the grass below them. This can be explained by the fact that the sun altitude is

5 quite high during the horizon scans and the trees are illuminated at a rather flat angle, while the grass is illuminated in a very steep angle. In that way, the local minimum at 0° can be explained. However, it is not clear why at shorter wavelengths no such increase of the measured signal towards smaller elevation angles is found. In order to investigate this in more detail, data from another MPIC instrument, which were collected during the first CINDI (CINDI-1) campaign, are used. At that time spectra at elevation sequences including very low (negative) elevation angles were recorded. Figure 23 shows ratios of spectra recorded

10 at elevation angles of −20°, −5° and −0.5° with respect to a 86° spectrum. These ratios indicate that systematically different spectral shapes are found for different elevation angles. For measurements close to the horizon, the spectral dependence is largest. In particular, it is much larger than found from satellite measurements. In other words, slightly below the horizon, the UV radiances are much lower than expected from satellite albedo measurements (assuming that the angle below the horizon points to vegetation). Interestingly, for a much lower elevation angle (−20°) the wavelength dependence is much weaker, and

15 also consistent with satellite based albedo measurements. The reason for this behaviour, however, is still not understood and should thus further investigated. This unexpected wavelength dependence of the elevation scans is another drawback of the horizon scans and if possible they should be analysed in the UV spectral range (at wavelenghts below ca. 370 nm).

4.3 Comparison between methods

Finally, the results for the far lamp measurements and horizon scans are compared for all instruments which recorded far lamp
20 spectra and performed a horizon scan on at least one day. For that, the mean horizon elevations are plotted against the corresponding mean lamp elevations. This plot is done separately for the horizon elevations retrieved at 340 nm and 440 nm since a systematic difference for the results at the two wavelengths was found for the horizon scans. However, no such dependency was found for the lamp measurements. The resulting correlation plots can be found in Fig. 24 and Fig. 25, respectively. The error bars in the x- and y-direction indicate the standard deviations of the retrieved lamp and horizon elevations, respectively.

25 A first finding is that the error bars are larger for the horizon scans. On the one hand, this can be explained by the larger number of horizon scan measurements since most of the groups performed lamp measurements only on one or two days. On the other hand, however, the horizon scans are probably more sensitive to the different weather conditions which influence the exact position of the apparent horizon. Furthermore, the horizon is not a homogenous line and therefore uncertainties arise from the uncertainty of the exact azimuth angles of the different instruments. Lastly, for many of the instruments the horizon

30 scans are performed at coarser resolution compared to the lamp scans, which also might effect the results and the resulting uncertainties.

In order to examine the consistency between the two methods, a total least squares (TLS) fit (Cantrell, 2008) is applied to the data. This fitting method takes the uncertainties of the obtained values in both x- and y-direction into account by weighting the values with respect to their uncertainties. In that way values with a smaller uncertainty get more weight compared to those with

a larger uncertainty. The resulting fit lines (solid red lines) with their corresponding slopes of 1.12 and 1.09 and their intercepts of 0.31° and 0.40° for 340 nm and 440 nm, respectively, are also displayed in the corresponding figures as well as the 1:1 line (dashed red line).

Taking all the uncertainties of the two different methods into account the slopes obtained by the TLS fits are close to 1 and
5 therefore, we can state that the results of the two methods correlate well. Nevertheless, the horizon is consistently seen at around 0.2° to 0.6° (except the CMA UV instrument which has a very large standard deviation in the horizon scans) higher elevations compared to the lamp scans which corresponds to around 4.5 m to 13 m at lamp distance. The consistent offset between horizon scans and lamp measurements is also represented by the intercepts of the TLS fits (0.31° and 0.40°). As already described in Sect. 3.6, this effect can be explained by the fact that during daytime the apparent horizon is probably represented by trees.
10 Finally, the difference of 0.1° in the offsets obtained for the two wavelengths is consistent with the findings from Sections 3.4 and 4.2.

All in all the two methods presented here yield consistent results for all of the instruments and therefore both are suited to calibrate the elevation angles of MAX-DOAS systems.

5 Overall discussion and conclusions

15 Four different methods for the calibration of elevations angles of MAX-DOAS instruments were described and discussed. All were applied during the CINDI-2 campaign by at least one group. The approaches of three methods were explained and examined using data from the MPIC MAX-DOAS instrument, while the near lamp measurements were described using data from the IUP-HD instrument. The white stripe measurements, using the MPIC setup, were only done for the MPIC instrument. The results of two methods, namely the horizon scans and the far lamp measurements, were inter-compared quantitatively
20 between the individual groups and amongst each other.

All of the methods use the same principle. First, a specific target is placed in front of the telescope unit of a MAX-DOAS system. This target has to be located at a fixed and known location relative to the optical unit of the instrument. In that way, an expected elevation angle β under which the target should be found can be determined. Then the apparent elevation angle $\widehat{\alpha}$ of the target is retrieved by the MAX-DOAS system using the measured intensities of an elevation scan across the target. Finally,
25 the elevation angles of the instrument are calibrated by comparing the expected and retrieved target positions and adjusting the telescope position in an appropriate way.

The first method used far lamp measurements during nighttime, where an artificial light source close to the horizon was used as the target. The results for the MPIC instrument illustrate the stability and reproducibility of this method since similar results are obtained for the different days at multiple wavelengths. The results of the other groups confirm this finding since a
30 rather small spread is found for each of the individual instruments. However, the spread of around 0.9° between all instruments is quite large, which is likely caused by the fact that the individual initial elevation calibrations are not done in a consistent way. All in all, the main advantages of this method are the stability, reproducibility and the possibility to calibrate several instruments with the same setup. Furthermore, this method is very accurate and precise. Looking at the standard deviation of

the retrieved lamp elevations of an individual instrument, the uncertainty of this method can be estimated as around ±0.05°. For many instruments, the uncertainty is even smaller and is finally limited by the precision of the motor of the instruments. Nevertheless, it might be difficult to find suitable lamp locations and to determine the position of the lamp relative to the telescope for most measurement sites. Therefore, the overall effort for this method is quite high. Lastly, this method can be

5 applied only during nighttime. It should be mentioned that this method can also be used for calibrating the azimuth angles of 2D instruments since also the azimuthal direction of the lamp can be determined, however, it might be difficult to find suitable lamp locations at different (azimuthal) locations.

Near lamp measurements offer another way to perform an elevation calibration. This method is very similar to the far lamp measurements and its main advantages are accuracy and stability. Furthermore, the setup is more compact and requires less

10 effort, especially in determining the position of the lamp relative to the telescope. However, when comparing the accuracy of the near and far lamp measurements, the distance between the lamp and the telescope is quite small for the near lamp measurements. This leads to a rather large angular fraction which is occupied by the lamp and might influence the results of the lamp scan. Therefore, we estimate the uncertainty of this method to be ±0.1°. Finally, this method can also be applied only during nighttime and only for one single instrument at once using the same setup.

15 Horizon scans during daytime use the visible horizon as target. Consistent results were found for all participating instruments compared to the far lamp measurements, represented by a good correlation of the retrieved horizon elevations for both methods. Here, the obtained slope is close to 1 and the obtained intercepts of 0.31° and 0.40° indicate an offset between lamp and horizon measurements. This offset can be explained by the fact that the visible horizon differed from the real horizon since obstacles such as trees represent the horizon during day. By knowing the height of these obstacles, this problem can

20 be solved. Additionally, it should be emphasised that the results of the horizon scans show a wavelength dependence (higher horizon elevations for larger wavelengths) which is likely caused by surface albedo effects and needs further investigation. The spread of the results for the different instruments is of the same order as for the far lamp measurements. However, the spread for the individual instruments is significantly larger than for the lamp measurements. This is probably caused by varying weather conditions leading to different horizon elevation results. Additionally, more horizon scans were performed, which

25 naturally increases the scatter in the retrieved horizon elevations since the scans were performed with different underlying sky conditions. The estimated uncertainty of the horizon scans is ±0.1° to ±0.3°, based on the standard deviations of the retrieved horizon elevations. Nevertheless, this method and its principle are quite simple and can be easily implemented in measurement protocols. Therefore, this method can be easily performed on a regular basis and used for monitoring the elevation calibration. One major drawback is the difficulty to determine the height of the visible horizon e.g. in mountainous regions. Also for com-

30 parison exercises it should be mentioned that the horizon is not a homogenous line but might have some inhomogeneities that can influence results for the individual instruments and therefore might introduce some discrepancies between the instruments.

White stripe measurements are another method which can be applied during the daytime. During the CINDI-2 campaign, the setup, which was used by MPIC, was rather experimental and measurements using this setup were performed only by the MPIC instrument. Nevertheless, the results are promising and consistent with the other methods and also other groups (e.g. BIRA)

35 applied this method utilising a different setup. Since the position of the stripe relative to the optical unit can be determined

very accurately, this method is very accurate. However, a stable setup is needed in order to perform a good calibration. For this method, we estimate an uncertainty on the order of ±0.1°, but since only one such measurement was performed by the MPIC instrument, further studies are needed in order to confirm this estimate.

The results of this study show that in principle all of the presented methods can be used for the calibration of the elevation
5   angles of MAX-DOAS systems since they yield consistent results. Nevertheless, the advantages and disadvantages of the individual methods should be considered when deciding for one method. A further finding of this study is the fact that still some improvement in the consistency of the elevation calibration between the different MAX-DOAS systems is needed as there is still a rather large discrepancy between the different instruments of around 1°. This is in the order of a typical FOV of a MAX-DOAS system and might have a significant effect on the retrieved MAX-DOAS trace gas dSCDs. Therefore, if
10 possible far lamp measurements should be performed at least once by all participating instruments and a common elevation reference (namely the lamp elevation) should be defined prior to a comparison campaign. Alternatively, near lamp or white stripe scans could be performed to accurately calibrate the elevation angles. However, these methods don't have a common reference elevation and might be more suitable for individual MAX-DOAS stations. Both, during campaigns and for single MAX-DOAS stations, horizon scans should be implemented in the measurement protocol and should be performed on a regular
15 basis in order to monitor the temporal stability of the calibration of the elevation angles.

Competing interests.   The authors declare that they have no conflict of interest.

Acknowledgements.   Funding for this study was provided by ESA through the CINDI-2 (ESA Contract No.4000118533/16/I-Sbo) and FRM4DOAS (FRM4DOAS: ESA Contract No. 4000118181/16/I-EF) projects and partly within the EU 7th Framework Programme QA4ECV (Grant Agreement no. 607405) project. The BOKU MAX-DOAS instrument was funded and the participation of S. F. Schreier was supported
20 by the Austrian Science Fund (FWF): I 2296-N29.

References

Apituley, A., Van Roozendael, M., et al.: Campaign overview..., in preparation, 2019.

Bruchkouski, I., Dziomin, V., and Krasouski, A.: Seasonal variability of the atmospheric trace constituents in Antarctica, 35th Canadian Symposium of Remote Sensing (IGARSS-2014), https://doi.org/10.1109/IGARSS.2014.6947387, https://ieeexplore.ieee.org/document/6947387, 2014.

Cantrell, C. A.: Technical Note: Review of methods for linear least-squares fitting of data and application to atmospheric chemistry problems, Atmospheric Chemistry and Physics, 8, 5477–5487, https://doi.org/10.5194/acp-8-5477-2008, https://www.atmos-chem-phys.net/8/5477/2008/, 2008.

Clémer, K., Van Roozendael, M., Fayt, C., Hendrick, F., Hermans, C., Pinardi, G., Spurr, R., Wang, P., and De Mazière, M.: Multiple wavelength retrieval of tropospheric aerosol optical properties from MAXDOAS measurements in Beijing, Atmospheric Measurement Techniques, 3, 863–878, https://doi.org/10.5194/amt-3-863-2010, https://www.atmos-meas-tech.net/3/863/2010/, 2010.

Donner, S.: Mobile MAX-DOAS measurements of the tropospheric formaldehyde column in the Rhein-Main region, Master's thesis, University of Mainz, Mainz, http://hdl.handle.net/11858/00-001M-0000-002C-EB17-2, 2016.

Drosoglou, T., Bais, A. F., Zyrichidou, I., Kouremeti, N., Poupkou, A., Liora, N., Giannaros, C., Koukouli, M. E., Balis, D., and Melas, D.: Comparisons of ground-based tropospheric NO_2 MAX-DOAS measurements to satellite observations with the aid of an air quality model over the Thessaloniki area, Greece, Atmospheric Chemistry and Physics, 17, 5829–5849, https://doi.org/10.5194/acp-17-5829-2017, https://www.atmos-chem-phys.net/17/5829/2017/, 2017.

Fraser, A., Adams, C., Drummond, J. R., Goutail, F., Manney, G., and Strong, K.: "The Polar Environment Atmospheric Research Laboratory UV–visible Ground-Based Spectrometer: First measurements of O_3, NO_2, BrO, and OClO columns", Journal of Quantitative Spectroscopy and Radiative Transfer, 110, 986–1004, https://doi.org/10.1016/j.jqsrt.2009.02.034, http://www.sciencedirect.com/science/article/pii/S0022407309000867, 2009.

Frieß, U., Monks, P., Remedios, J., Rozanov, A., Sinreich, R., Wagner, T., and Platt, U.: MAX-DOAS O_4 measurements: A new technique to derive information on atmospheric aerosols: 2. Modeling studies, Journal of Geophysical Research: Atmospheres, 111, https://doi.org/10.1029/2005JD006618, 2006.

Frieß, U., Klein Baltink, H., Beirle, S., Clémer, K., Hendrick, F., Henzing, B., Irie, H., de Leeuw, G., Li, A., Moerman, M. M., van Roozendael, M., Shaiganfar, R., Wagner, T., Wang, Y., Xie, P., Yilmaz, S., and Zieger, P.: Intercomparison of aerosol extinction profiles retrieved from MAX-DOAS measurements, Atmospheric Measurement Techniques, 9, 3205–3222, https://doi.org/10.5194/amt-9-3205-2016, https://www.atmos-meas-tech.net/9/3205/2016/, 2016.

Hönninger, G. and Platt, U.: Observations of BrO and its vertical distribution during surface ozone depletion at Alert, Atmospheric Environment, 36, 2481–2489, 2002.

Hönninger, G., von Friedeburg, C., and Platt, U.: Multi axis differential optical absorption spectroscopy (MAX-DOAS), Atmospheric Chemistry and Physics, 4, 231–254, https://doi.org/10.5194/acp-4-231-2004, https://www.atmos-chem-phys.net/4/231/2004/, 2004.

Irie, H., Kanaya, Y., Akimoto, H., Iwabuchi, H., Shimizu, A., and Aoki, K.: First retrieval of tropospheric aerosol profiles using MAX-DOAS and comparison with lidar and sky radiometer measurements, Atmospheric Chemistry and Physics, 8, 341–350, https://doi.org/10.5194/acp-8-341-2008, https://www.atmos-chem-phys.net/8/341/2008/, 2008.

Kreher, K., Van Roozendael, M., Hendrick, F., Apituley, A., Dimitropoulou, E., Frieß, U., Richter, A., Wagner, T., Abuhassan, N., Ang, L., Anguas, M., Bais, A., Benavent, N., Bösch, T., Bognar, K., Borovski, A., Bruchkousky, I., Cede, A., Chan, K. L., Donner, S., Drosoglou,

T., Fayt, C., Finkenzeller, H., Garcia-Nieto, D., Gielen, C., Gómez-Martín, L., Hao, N., Hermans, C., Hoque, S., Irie, H., Jin, J., Johnston, P., Khayyam Butt, J., Khokhar, F., Koenig, T. K., Kuhn, J., Kumar, V., Lampel, J., Liu, C., Ma, J., Merlaud, A., Mishra, A. K., Müller, M., Navarro-Comas, M., Ostendorf, M., Pazmino, A., Peters, E., Pinardi, G., Pinharanda, M., Piters, A., Platt, U., Postylyakov, O., Prados-Roman, C., Puentedura, O., Querel, R., Saiz-Lopez, A., Sinha, V., Schönhardt, A., Schreier, S. F., Seyler, A., Spinei, E., Strong, K., Tack, F., Tiefengraber, M., Tirpitz, J.-L., van Gent, J., Volkamer, R., Vrekoussis, M., Wang, S., Wang, Z., Wenig, M., Wittrock, F., Xie, P., Xu, J., Yela, M., Zhang, C., and Zhao, X.: Intercomparison of NO_2, O_4, O_3 and HCHO slant column measurements by MAX-DOAS and zenith-sky UV-Visible spectrometers during the CINDI-2 campaign, in preparation, 2019.

Lampel, J., Frieß, U., and Platt, U.: The impact of vibrational Raman scattering of air on DOAS measurements of atmospheric trace gases, Atmospheric Measurement Techniques, 8, 3767–3787, https://doi.org/10.5194/amt-8-3767-2015, https://www.atmos-meas-tech.net/8/3767/2015/, 2015.

Peters, E., Wittrock, F., Großmann, K., Frieß, U., Richter, A., and Burrows, J. P.: Formaldehyde and nitrogen dioxide over the remote western Pacific Ocean: SCIAMACHY and GOME-2 validation using ship-based MAX-DOAS observations, Atmospheric Chemistry and Physics, 12, 11 179–11 197, https://doi.org/10.5194/acp-12-11179-2012, https://www.atmos-chem-phys.net/12/11179/2012/, 2012.

Pinardi, G., Van Roozendael, M., Abuhassan, N., Adams, C., Cede, A., Clémer, K., Fayt, C., Frieß, U., Gil, M., Herman, J., Hermans, C., Hendrick, F., Irie, H., Merlaud, A., Navarro Comas, M., Peters, E., Piters, A. J. M., Puentedura, O., Richter, A., Schönhardt, A., Shaiganfar, R., Spinei, E., Strong, K., Takashima, H., Vrekoussis, M., Wagner, T., Wittrock, F., and Yilmaz, S.: MAX-DOAS formaldehyde slant column measurements during CINDI: intercomparison and analysis improvement, Atmospheric Measurement Techniques, 6, 167–185, https://doi.org/10.5194/amt-6-167-2013, https://www.atmos-meas-tech.net/6/167/2013/, 2013.

Piters, A. J. M., Boersma, K. F., Kroon, M., Hains, J. C., Van Roozendael, M., Wittrock, F., Abuhassan, N., Adams, C., Akrami, M., Allaart, M. A. F., Apituley, A., Beirle, S., Bergwerff, J. B., Berkhout, A. J. C., Brunner, D., Cede, A., Chong, J., Clémer, K., Fayt, C., Frieß, U., Gast, L. F. L., Gil-Ojeda, M., Goutail, F., Graves, R., Griesfeller, A., Großmann, K., Hemerijckx, G., Hendrick, F., Henzing, B., Herman, J., Hermans, C., Hoexum, M., van der Hoff, G. R., Irie, H., Johnston, P. V., Kanaya, Y., Kim, Y. J., Klein Baltink, H., Kreher, K., de Leeuw, G., Leigh, R., Merlaud, A., Moerman, M. M., Monks, P. S., Mount, G. H., Navarro-Comas, M., Oetjen, H., Pazmino, A., Perez-Camacho, M., Peters, E., du Piesanie, A., Pinardi, G., Puentedura, O., Richter, A., Roscoe, H. K., Schönhardt, A., Schwarzenbach, B., Shaiganfar, R., Sluis, W., Spinei, E., Stolk, A. P., Strong, K., Swart, D. P. J., Takashima, H., Vlemmix, T., Vrekoussis, M., Wagner, T., Whyte, C., Wilson, K. M., Yela, M., Yilmaz, S., Zieger, P., and Zhou, Y.: The Cabauw Intercomparison campaign for Nitrogen Dioxide measuring Instruments (CINDI): design, execution, and early results, Atmospheric Measurement Techniques, 5, 457–485, https://doi.org/10.5194/amt-5-457-2012, https://www.atmos-meas-tech.net/5/457/2012/, 2012.

Roscoe, H. K., Van Roozendael, M., Fayt, C., du Piesanie, A., Abuhassan, N., Adams, C., Akrami, M., Cede, A., Chong, J., Clémer, K., Friess, U., Gil Ojeda, M., Goutail, F., Graves, R., Griesfeller, A., Grossmann, K., Hemerijckx, G., Hendrick, F., Herman, J., Hermans, C., Irie, H., Johnston, P. V., Kanaya, Y., Kreher, K., Leigh, R., Merlaud, A., Mount, G. H., Navarro, M., Oetjen, H., Pazmino, A., Perez-Camacho, M., Peters, E., Pinardi, G., Puentedura, O., Richter, A., Schönhardt, A., Shaiganfar, R., Spinei, E., Strong, K., Takashima, H., Vlemmix, T., Vrekoussis, M., Wagner, T., Wittrock, F., Yela, M., Yilmaz, S., Boersma, F., Hains, J., Kroon, M., Piters, A., and Kim, Y. J.: Intercomparison of slant column measurements of NO_2 and O_4 by MAX-DOAS and zenith-sky UV and visible spectrometers, Atmospheric Measurement Techniques, 3, 1629–1646, https://doi.org/10.5194/amt-3-1629-2010, https://www.atmos-meas-tech.net/3/1629/2010/, 2010.

Schreier, S. F. et al.: Multiple ground-based MAX-DOAS observations in Vienna, Austria – part 1: Evaluation of horizontal and temporal NO_2, HCHO, and CHOCHO distributions and comparison with independent data sets, to be submitted to Atmospheric Chemistry and Physics, 2019.

Van Roozendael, M., Fayt, C., Post, P., Hermans, C., and Lambert, J. C.: Retrieval of Tropospheric BrO and NO_2 from UV-Visible Observations, pp. 155–165, Springer, Heidelberg, https://doi.org/10.1007/978-3-642-18875-6_19, 2004.

Wagner, T., Dix, B., Friedeburg, C. v., Frieß, U., Sanghavi, S., Sinreich, R., and Platt, U.: MAX-DOAS O_4 measurements - a new technique to derive information on atmospheric aerosols, (I) Principles and information content, Journal of Geophysical Research: Atmospheres,

5   109, https://doi.org/10.1029/2004JD004904, https://agupubs.onlinelibrary.wiley.com/doi/abs/10.1029/2004JD004904, 2004.

Wagner, T., Beirle, S., Brauers, T., Deutschmann, T., Frieß, U., Hak, C., Halla, J. D., Heue, K. P., Junkermann, W., Li, X., Platt, U., and Pundt-Gruber, I.: Inversion of tropospheric profiles of aerosol extinction and HCHO and NO_2 mixing ratios from MAX-DOAS observations in Milano during the summer of 2003 and comparison with independent data sets, Atmospheric Measurement Techniques, 4, 2685–2715, https://doi.org/10.5194/amt-4-2685-2011, https://www.atmos-meas-tech.net/4/2685/2011/, 2011.

10   Wittrock, F., Oetjen, H., Richter, A., Fietkau, S., Medeke, T., Rozanov, A., and Burrows, J. P.: MAX-DOAS measurements of atmospheric trace gases in Ny-Ålesund - Radiative transfer studies and their application, Atmospheric Chemistry and Physics, 4, 955–966, https://doi.org/10.5194/acp-4-955-2004, https://www.atmos-chem-phys.net/4/955/2004/, 2004.

Table 1. Overview of the groups that participated in the elevation calibration exercise. The table lists the institute names, the corresponding instrument names, their instrument acronyms, and their respective instrument IDs which were used during the CINDI-2 campaign and in some plots of this paper.

Institute	Instrument name	Instrument acronym	Instrument ID
Anhui Institute of Optics and Fine Mechanics	2D-MAXDOAS	AIOFM	aiofm_1
Aristotle University of Thessaloniki	PHAETHON	AUTH	auth_3
Royal Belgian Institute for Space Aeronomy	2D-MAXDOAS	BIRA	bira_4
University of Natural Resources and Life Sciences Vienna	2D-MAXDOAS	BOKU	boku_6
Belarusian State University	MARSB	BSU	bsu_5
China Meteorological Administration	MiniDOAS UV/ VIS	CMA UV/ CMA VIS	cma_7/ cma_8
University of Bremen	2D-MAXDOAS	IUP-B	iupb_18
University of Heidelberg	2D-EnviMes	IUP-HD	iuph_19
Ludwig-Maximilians-Universität München	2D-EnviMes	LMU	lmumim_35
Max Planck Institute for Chemistry	Tube MAX-DOAS	MPIC	mpic_28
University of Toronto	2D-MAXDOAS	UToronto	uto_36

Table 2. Overview of the key properties of the instruments participating in the elevation calibration exercise. The table lists the instrument acronyms as defined in Table 1, the instrument types (1D/2D) as well as the spectral range and resolution for each instrument (columns 1-4). Further, the number of detectors and light couplings, the type of light coupling (fibre F or direct D) and the instrument fields of view (FOV) are specified (columns 5-7). Finally, the corresponding detector temperatures and references explaining the individual instruments in more detail are given (columns 8-9).

Instrument	Type	Spectral range (nm)	Spectral resolution (nm)	Number of detectors/ couplings	Light coupling	FOV (°)	Detector temperature (°C)	Reference
AIOFM	2D	290-380	0.4	1/ 1	F	0.2	-30	N/A
AUTH	2D	300-450	0.4	1/ 1	F	1.0	5	Drosoglou et al. (2017)
BIRA	2D	300-390/ 400-560	0.37/ 0.58	2/ 2	F	1.0/ 0.5	-50/ -50	Clémer et al. (2010)
BOKU	2D	419-553	0.8	1/ 1	F	0.8	-60	Schreier et al. (2019)
BSU	1D	300-500	0.4	1/ 1	D	0.2-1.0	-40	Bruchkouski et al. (2014)
CMA UV	1D	300-450	0.7	1 /1	F	0.8	room	N/A
CMA VIS	1D	400-710	1.6	1/ 1	F	0.8	room	N/A
IUP-B	2D	305-390/ 406-579	0.45/ 0.83	2/ 1	F	1.0	-35/ -30	Peters et al. (2012)
IUP-HD	2D	300-460/ 440-580	0.6/ 0.5	2/ 1	F	<0.5	20	Lampel et al. (2015)
LMU	2D	300-460/ 450-600	0.6/ 0.9	2/ 1	F	0.4	20	Lampel et al. (2015)
MPIC	1D	305-465	0.6	1/ 1	F	0.7	20	Donner (2016)
UToronto	2D	340-560	0.75	1/ 1	F	0.62	-70	Fraser et al. (2009)

Table 3. Overview of the lamp elevations obtained for all days and different wavelengths for the MPIC instrument. Additionally, the scan resolution is indicated in the last column.

Date	365.16 nm	404.90 nm	435.96 nm	Resolution
08.09.	−0.15°	−0.16°	−0.19°	0.10°
10.09.	−0.01°	−0.01°	−0.01°	0.02°
13.09.	0.01°	0.02°	0.02°	0.02°
19.09.	0.01°	0.02°	0.02°	0.02°

Table 4. Overview of the retrieved target elevations $\hat{\alpha}$ for the MPIC instrument using three of the methods described in the text.

Method	Target elevation
Far lamp	−0.01° to 0.02°
Horizon scans	0.22° to 0.41°
White stripe	−0.02° to 0.02°

Table 5. Overview of the mean and median horizon elevations for the instruments located on the upper and lower roof containers and their corresponding standard deviations (STD).

Row	Mean (°)	Median (°)	STD (°)
Upper 440 nm	0.21	0.18	0.19
Upper 340 nm	0.14	0.11	0.17
Lower 440 nm	0.13	0.06	0.26
Lower 340 nm	0.03	0.06	0.26
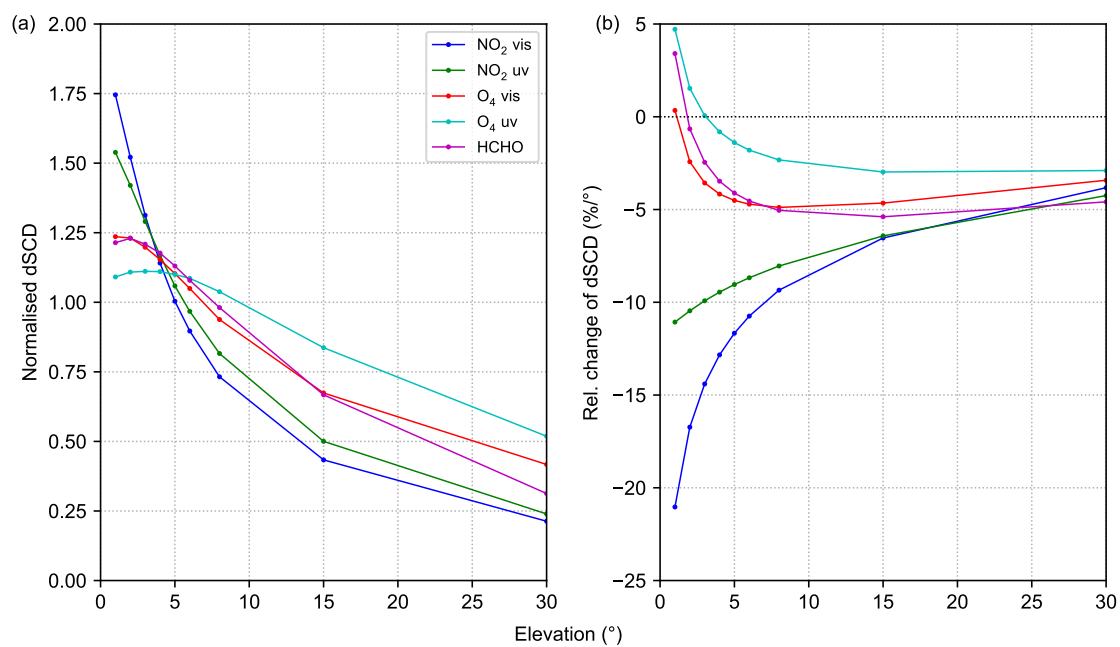
Figure 1. (a) Mean dependence of the trace gas dSCDs on the elevation angle for the whole campaign. Each curve was normalised to the mean dSCD value of the elevation sequence. (b) Relative change of the measured dSCDs per degree pointing error at different elevation angles.
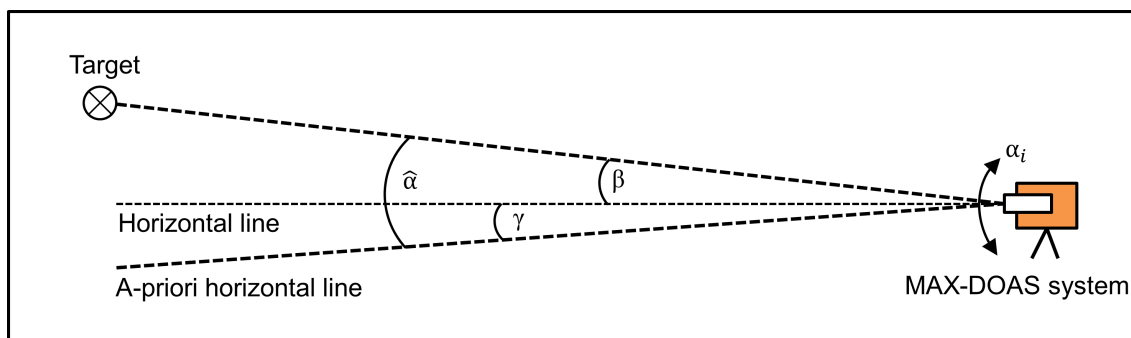
Figure 2. Sketch of the general experimental setup and angle definition used in this study.
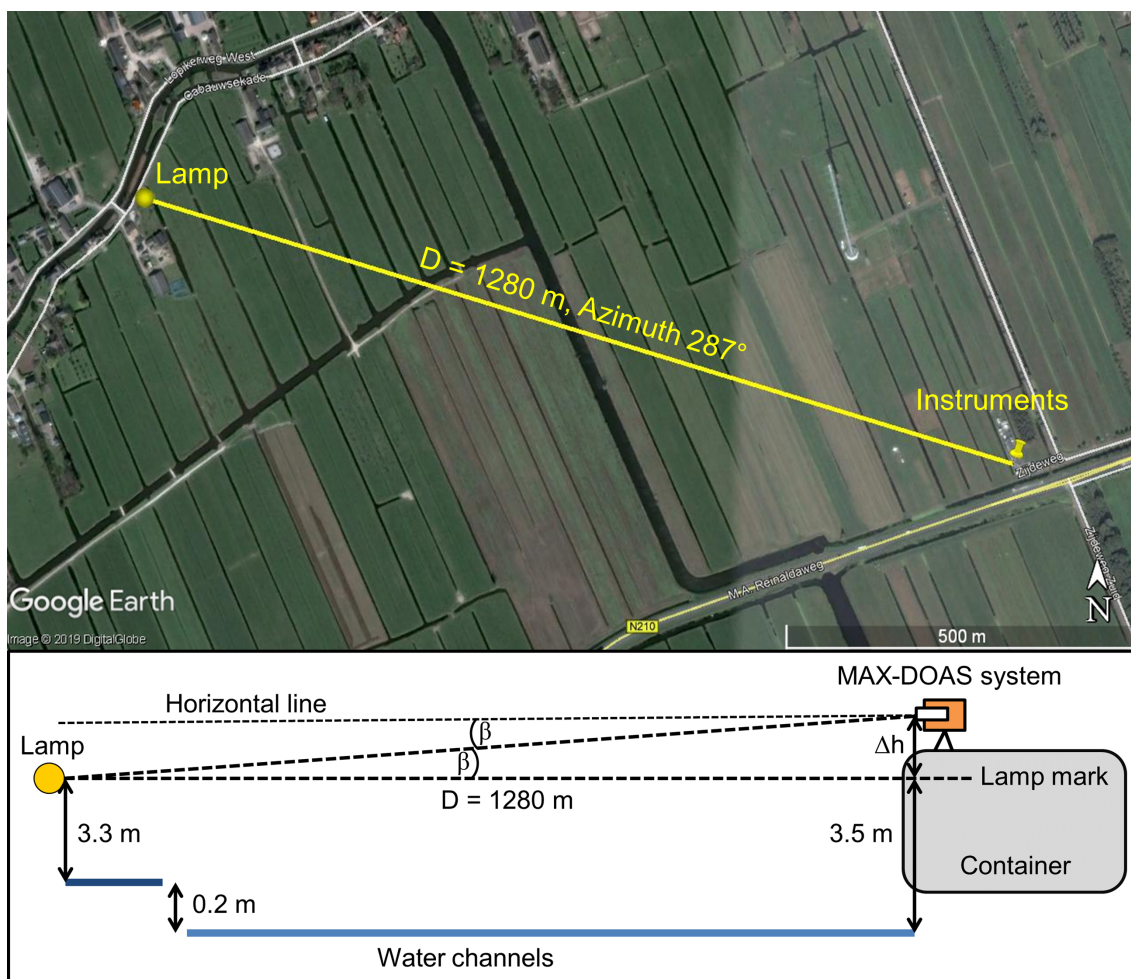
Figure 3. Upper part: map indicating the position of both the lamp and the MAX-DOAS instruments. Lower part: sketch of the setup for the far lamp measurements during the CINDI-2 campaign.
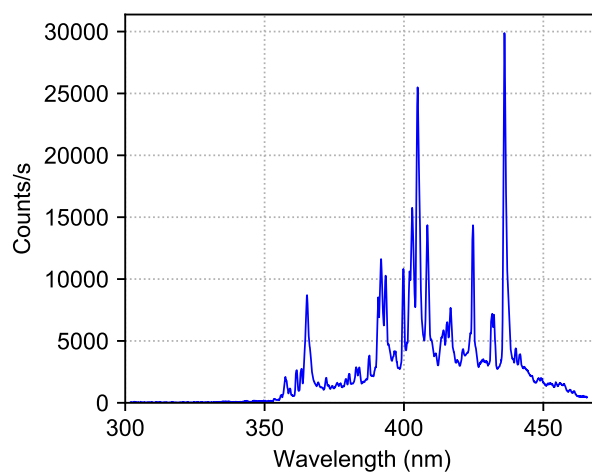
Figure 4. Xenon lamp spectrum recorded on 13th September 2016 by the MPIC instrument. The three distinct emission lines at 365.16 nm, 404.90 nm and 435.96 nm which are used for the analysis are clearly visible.
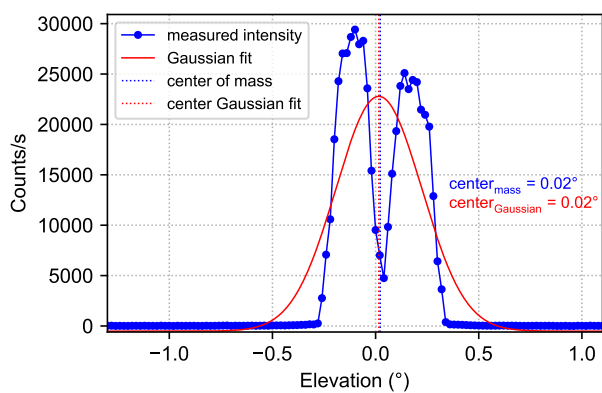
Figure 5. Intensity curve at 435.96 nm (blue solid line) recorded on 13th September by the MPIC instrument. The obtained center of mass is indicated by the blue dashed line. Further, the center obtained by a Gaussian fit and the corresponding fit are displayed in red.
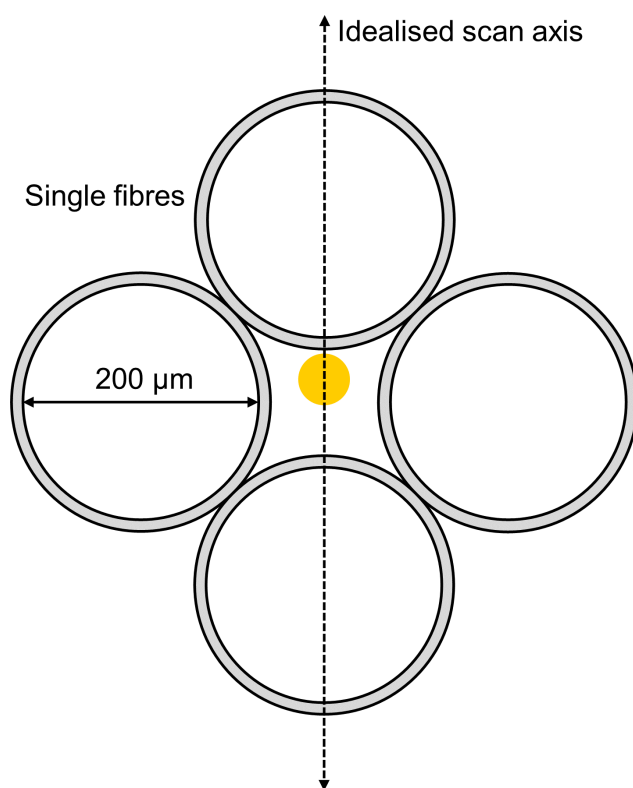
Figure 6. Sketch of the fibre bundle placed in the focal point of the telescope of the MPIC instrument. The grey parts indicate the gladding (additional 20 μm) of the fibres. The white circles represent the light-conducting part of the single glass fibres with a diameter of 200 μm, while the yellow spot indicates the idealised image (neglecting aberration etc.) of the xenon lamp inside the telescope which has a diameter of 7 μm. Note, that the size of the yellow dot is not shown at the correct scale relative to the fibre diameter and is larger than in reality.
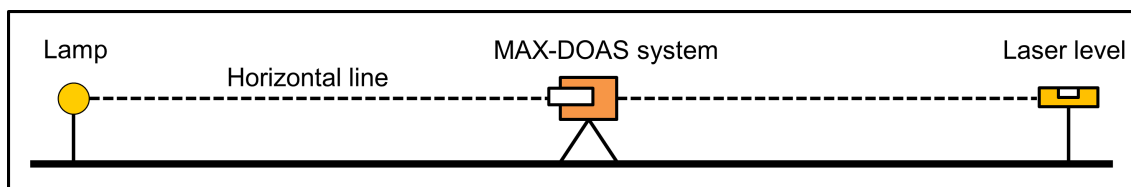
Figure 7. Sketch of the measurement setup for the near lamp measurements and the alignment of telescope and lamp.
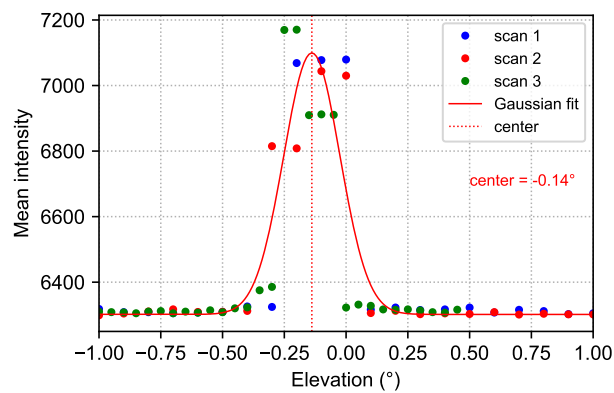
Figure 8. Measured intensities for the three individual scans (coloured dots) and the fitted Gaussian (red solid line) obtained from the near lamp measurements by the IUP-HD instrument in the UV spectral range.
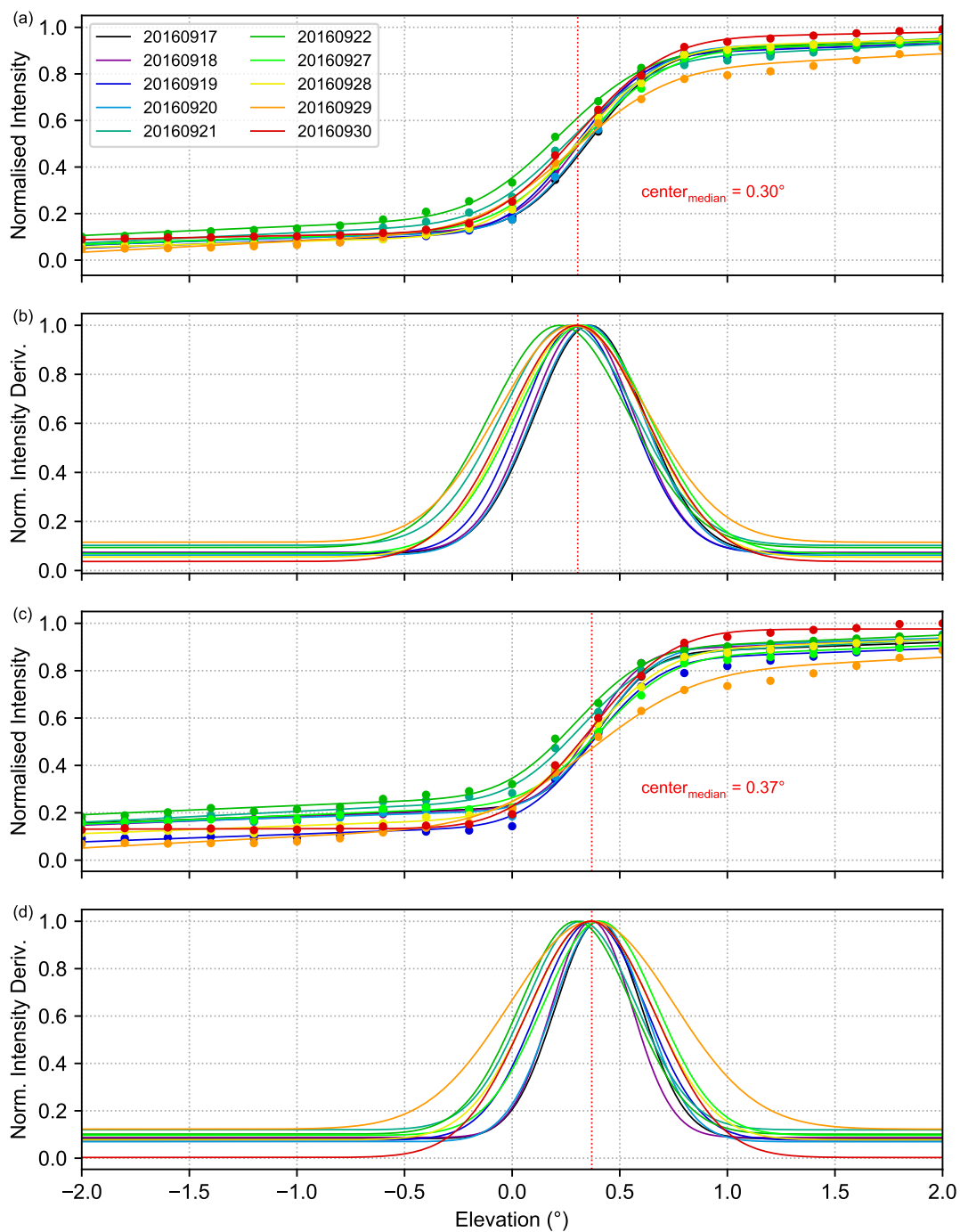
Figure 9. (a) and (c) Normalised intensity curves for the horizon scans performed by the MPIC instrument throughout the campaign at 340 nm and 440 nm, respectively. The coloured solid lines indicate the respective Gaussian integral fits. (b) and (d) Normalised derivatives of the respective intensity curves.
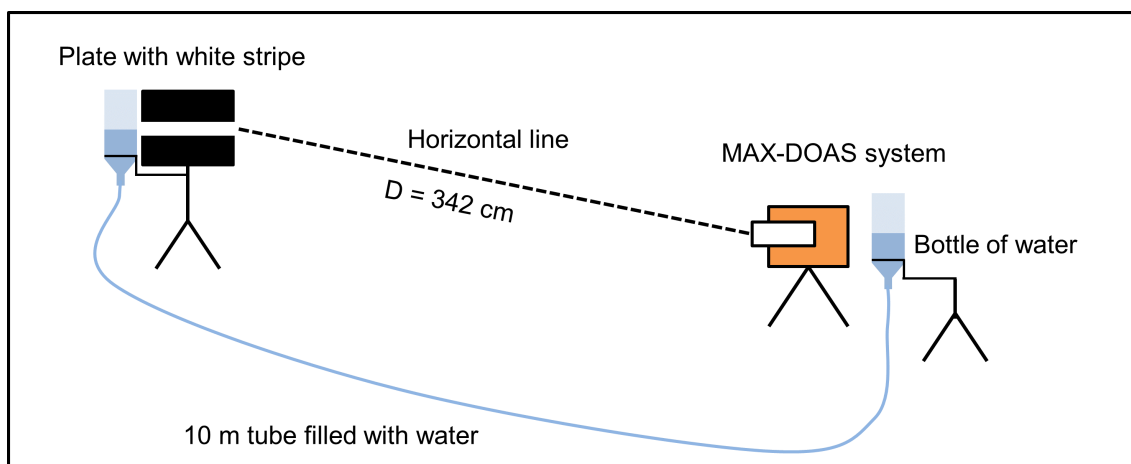
Figure 10. Sketch of the measurement setup used by MPIC for the white stripe scans and the alignment of the telescope and white stripe using a water level.
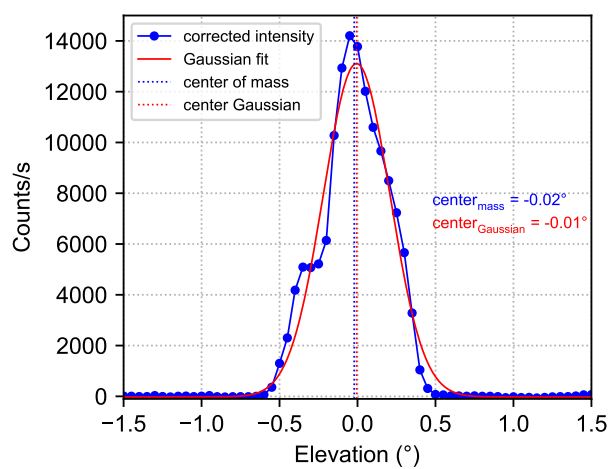
Figure 11. Background corrected intensity curve at 440 nm and corresponding Gaussian fit for the white stripe scan on 20th September performed by the MPIC instrument. The retrieved apparent stripe positions for the two methods are indicated by the dashed lines.
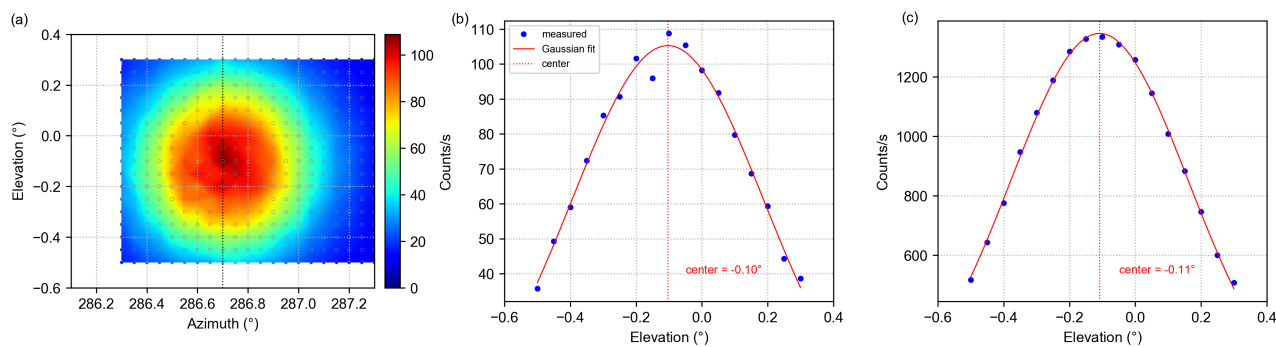
Figure 12. (a) Example of the 2D intensity distribution at 365 nm measured on 10th September by the BIRA UV instrument. Panels (b) and (c) show the corresponding transect along the black dashed line in (a) and the azimuthal sum of the intensities at the different elevations, respectively. Additionally, the respective Gaussian fits and their centers are indicated.
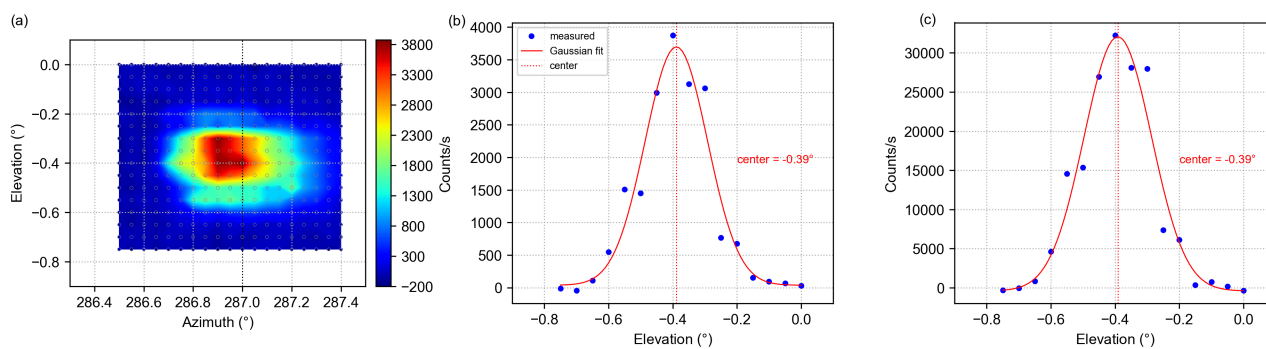
Figure 13. (a) Example of the 2D intensity distribution at 365 nm measured on 13th September by the IUP-HD UV instrument. Panels (b) and (c) show the corresponding transect along the black dashed line in (a) and the azimuthal sum of the intensities at the different elevations, respectively. Additionally, the respective Gaussian fits and their centers are indicated.
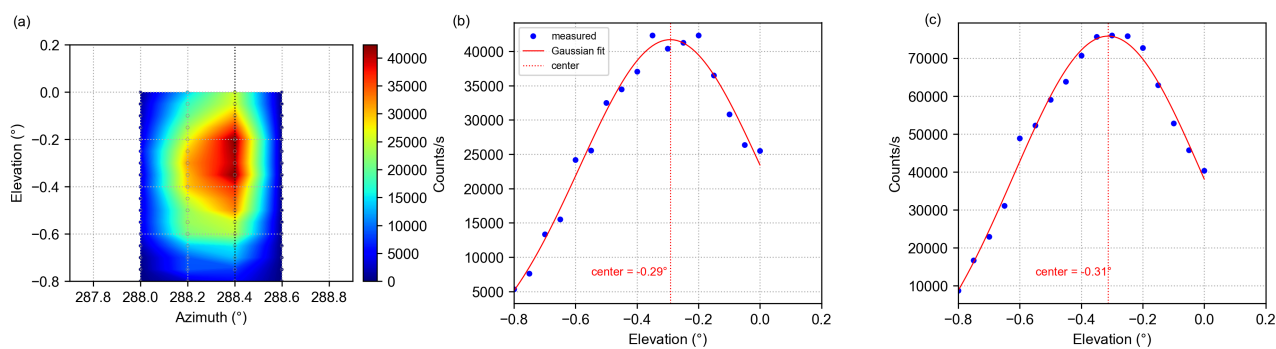
Figure 14. (a) Example of the 2D intensity distribution at 436 nm measured on 10th September by the UToronto instrument. Panels (b) and (c) show the corresponding transect along the black dashed line in (a) and the azimuthal sum of the intensities at the different elevations, respectively. Additionally, the respective Gaussian fits and their centers are indicated.
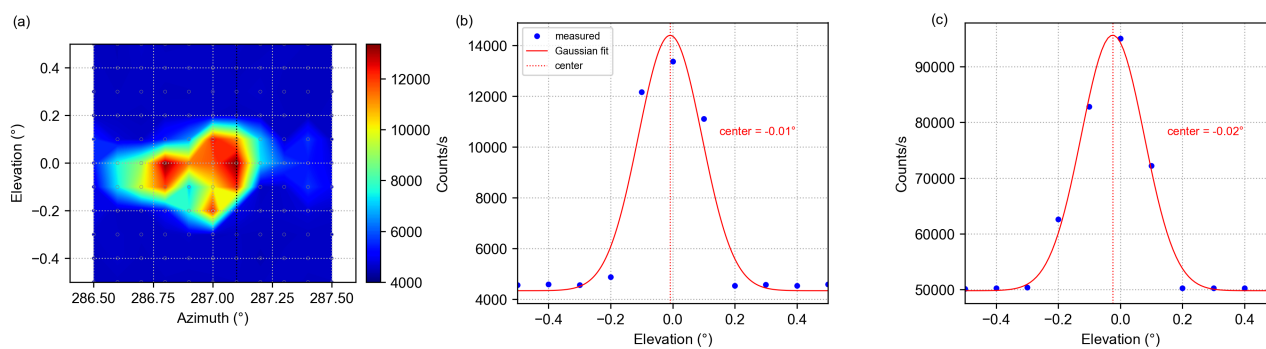
Figure 15. (a) Example of the 2D intensity distribution (mean intensity) measured on 10th September by the LMU instrument. Panels (b) and (c) show the corresponding transect along the black dashed line in (a) and the azimuthal sum of the intensities at the different elevations, respectively. Additionally, the respective Gaussian fits and their centers are indicated.
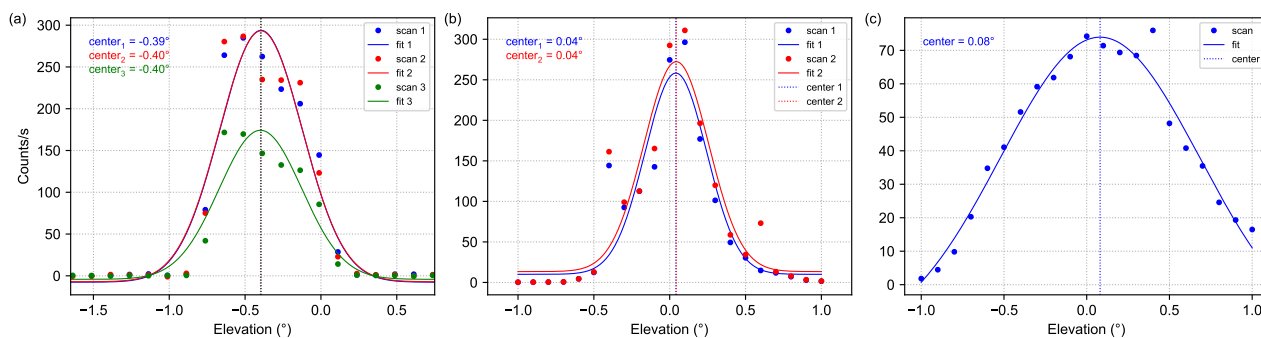
Figure 16. (a) Intensity curves at 365 nm recorded on 10th September by the AUTH instrument. (b) Intensity curves at 546 nm recorded on 13th September by the BOKU instrument. (c) Intensity curve at 546 nm recorded on 13th September by the IUP-B visible instrument.
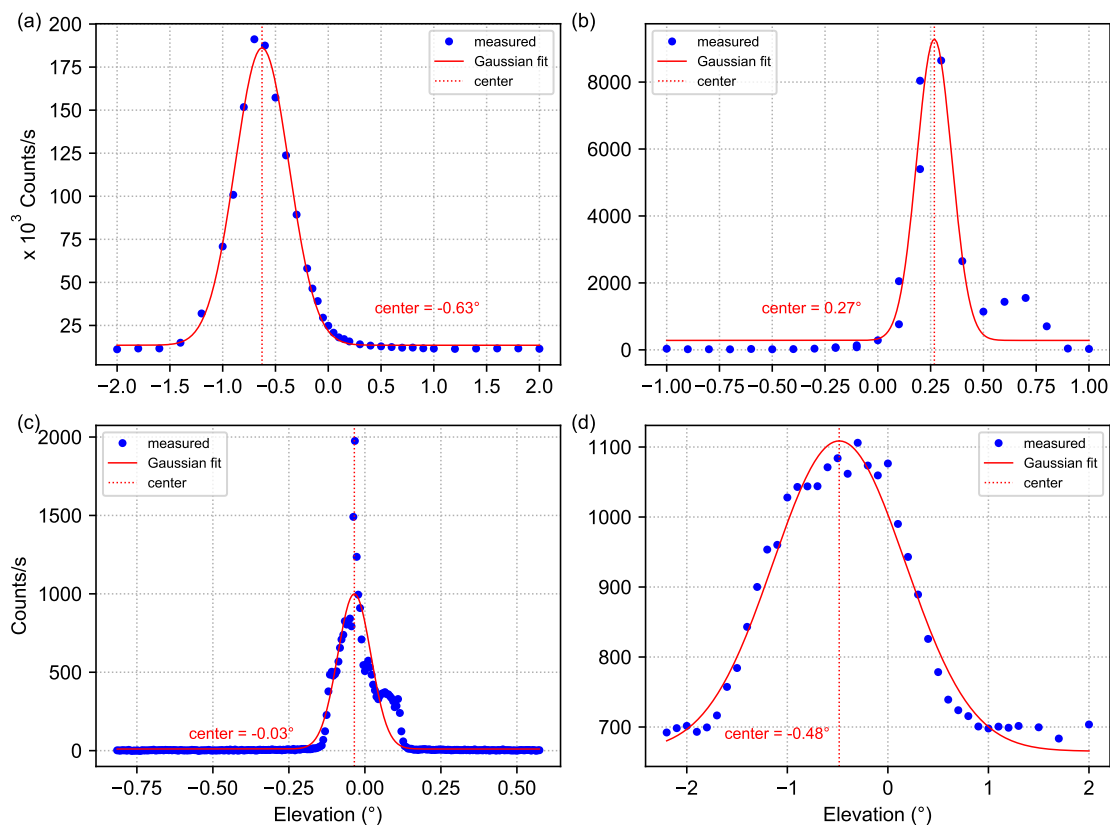
Figure 17. (a) Intensity curve at 436 nm recorded on 19th September by the CMA UV instrument. (b) Intensity curve at 546 nm recorded on 19th September by the CMA VIS instrument. (c) Intensity curve at 365 nm recorded on 10th September by the BSU instrument. (d) Intensity curve at 365 nm recorded on 8th September by the AIOFM instrument.
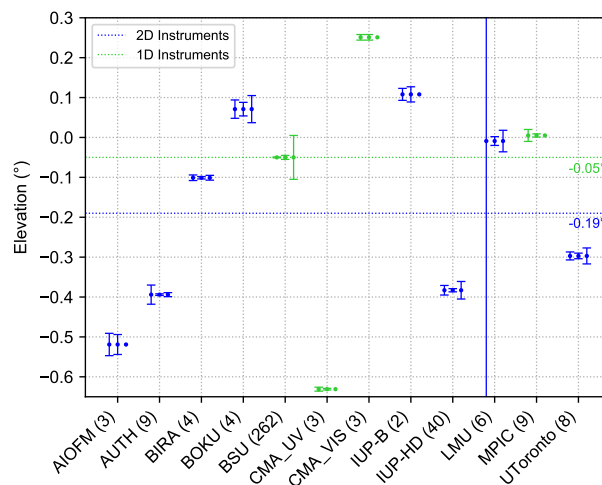
Figure 18. Overview of the retrieved lamp elevations for the 2D and 1D instruments including different measures of their uncertainty, mean of fit errors (left), error of the mean (middle) and daily spread (right). The number of available lamp scans for each instrument is displayed in brackets after the individual institute acronyms. The expected lamp elevations are indicated by the corresponding dashed lines.
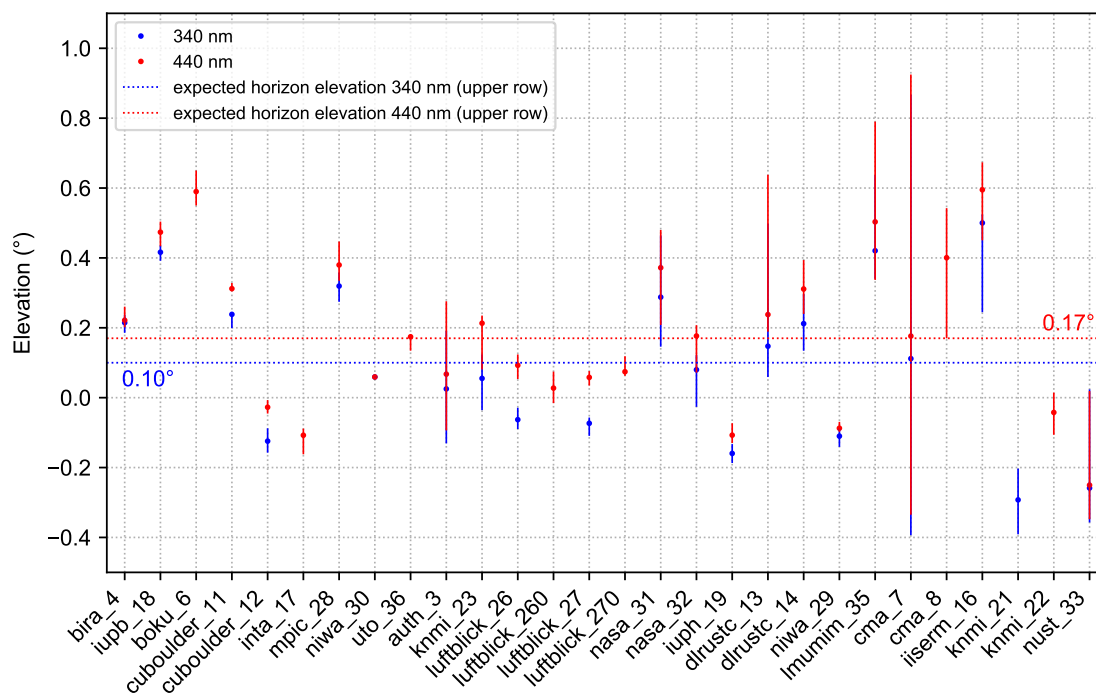
Figure 19. Overview of the retrieved median horizon elevations for all participating instruments at the two different wavelengths. Additionally, the 25 % and 75 % percentiles are indicated by the lines.
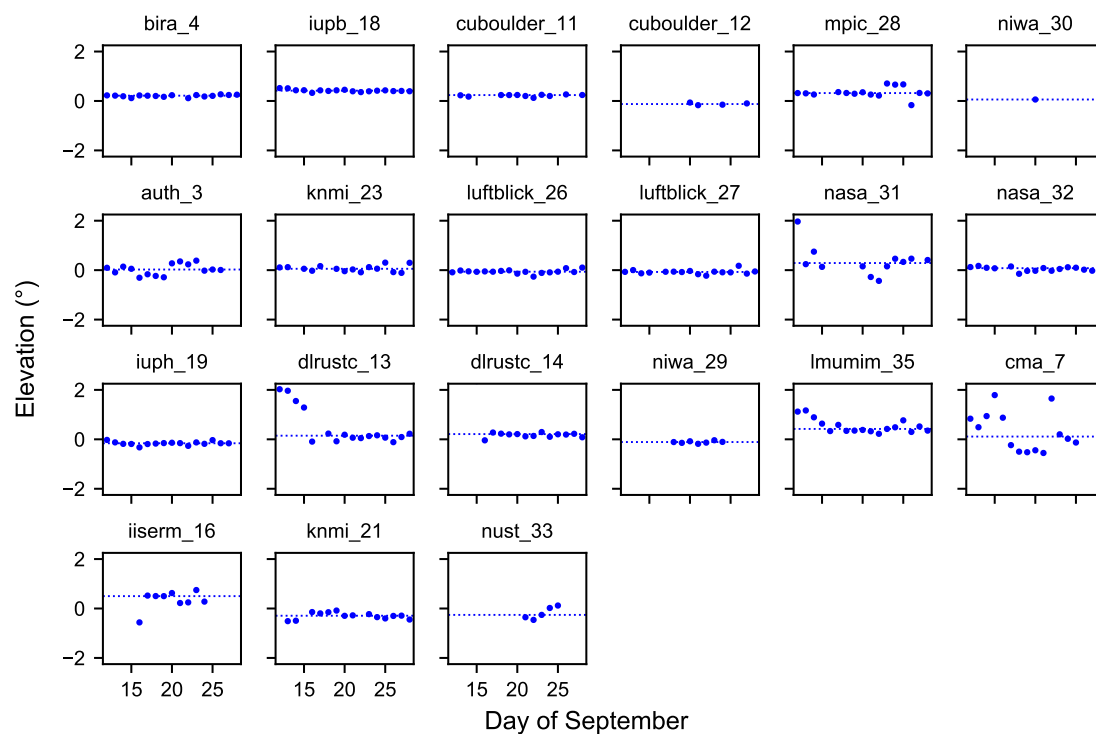
Figure 20. Overview of the daily results of the horizon scans for all participating instruments at 340 nm. Additionally, in each subplot the median horizon elevation for the corresponding instrument is indicated by a dashed line.
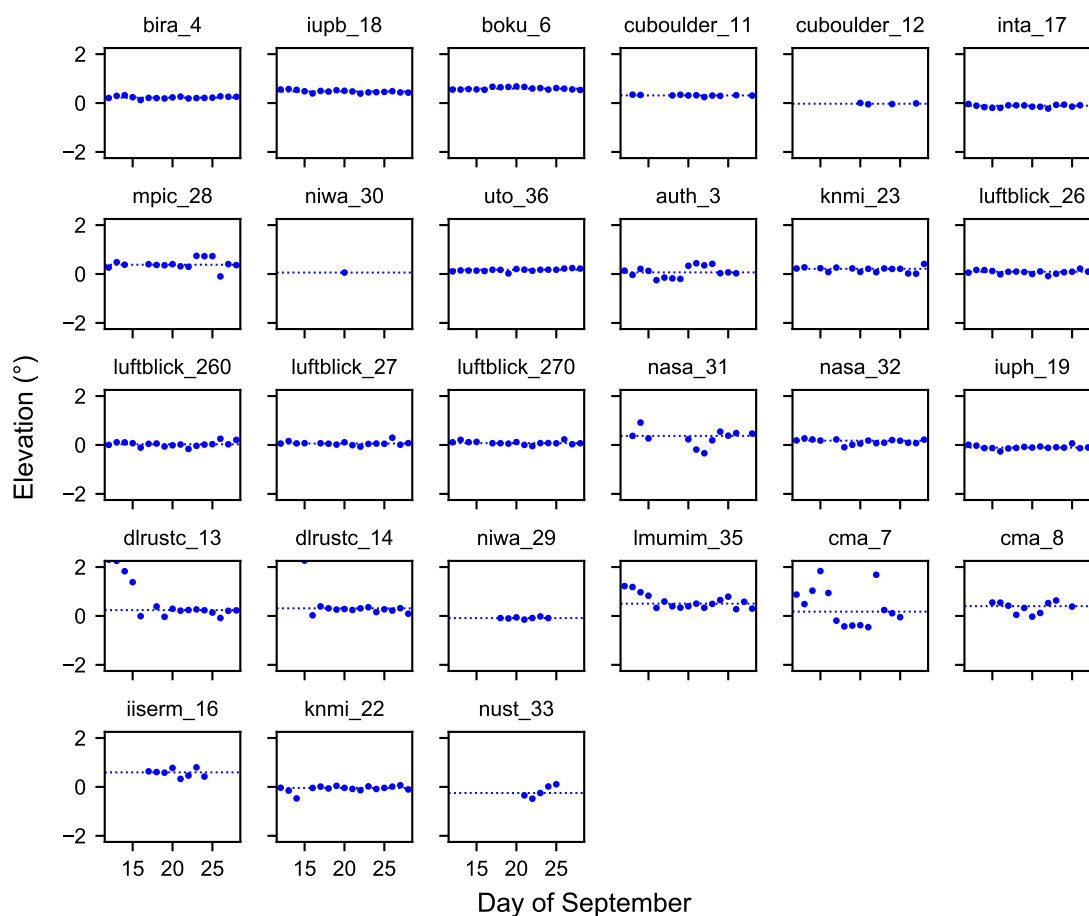
Figure 21. Overview of the daily results of the horizon scans for all participating instruments at 440 nm. Additionally, in each subplot the median horizon elevation for the corresponding instrument is indicated by a dashed line.
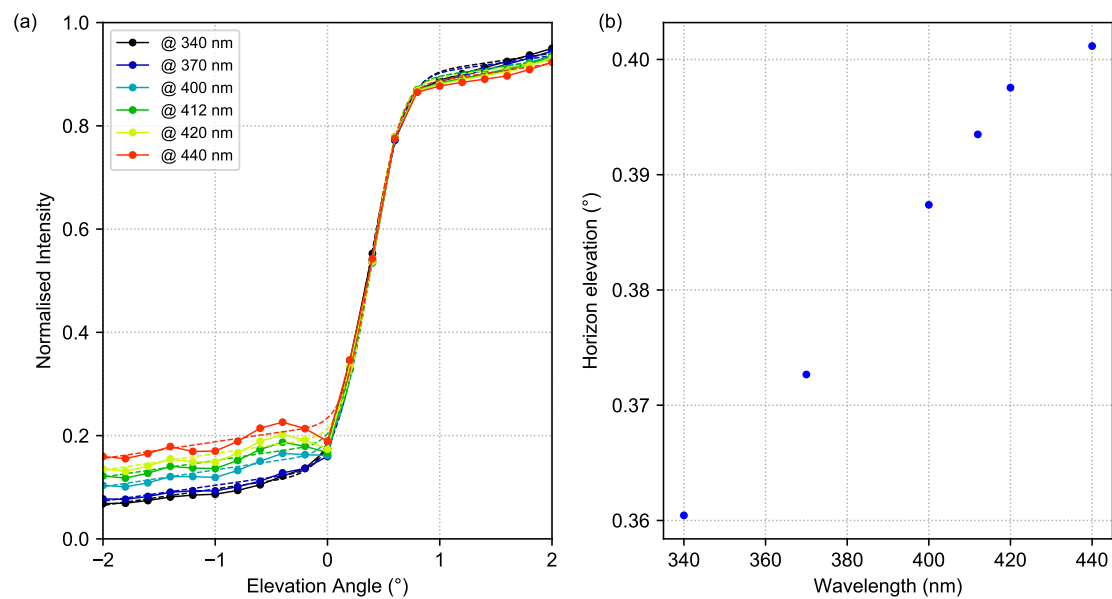
Figure 22. (a) Normalised intensity curves (coloured dots) and corresponding Gaussian integral fits (coloured dashed lines) at different wavelengths for the horizon scan performed on 17th September by the MPIC instrument. (b) Respective horizon elevations (retrieved from the fits in (a)) as a function of wavelength.
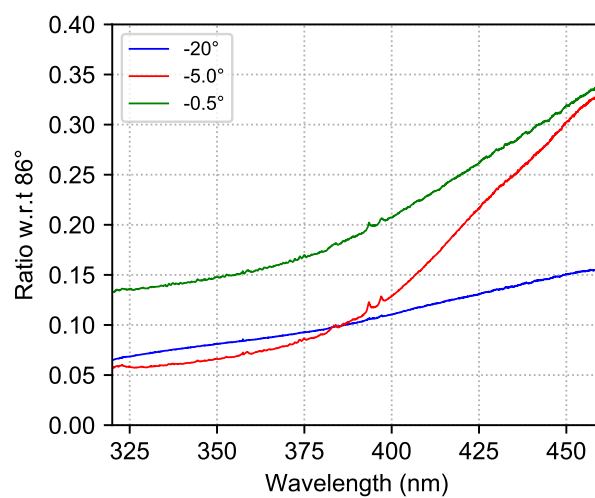
Figure 23. Ratios with respect to a 86° spectrum for spectra measured at −20°, −5° and −0.5°, respectively, during the CINDI-1 campaign by the MPIC MAX-DOAS instrument.
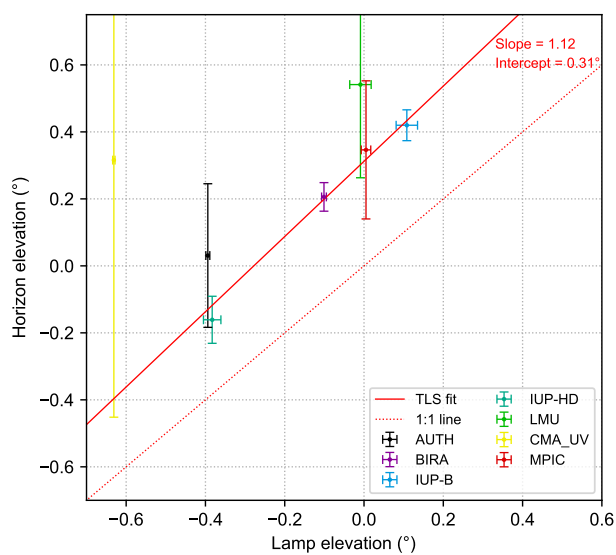
Figure 24. Correlation between retrieved horizon (at 340 nm) and lamp elevations for all participating instruments that reported results for both methods. The error bars indicate the standard deviations of the retrieved lamp and horizon elevations. Further, the result of a TLS fit and the 1:1 line are shown.
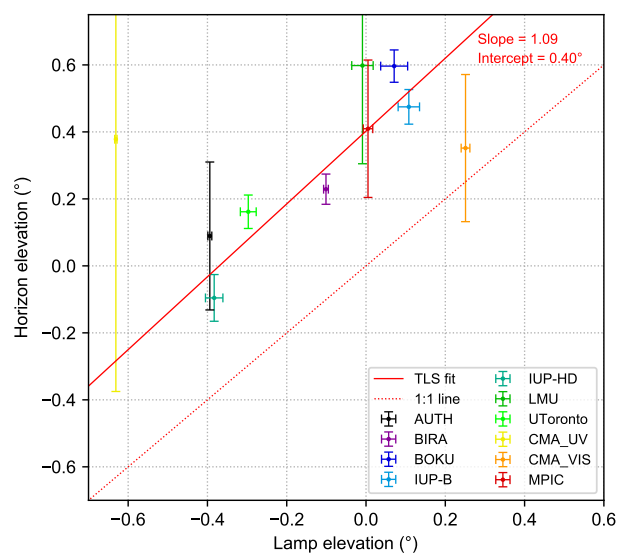
Figure 25. Correlation between retrieved horizon (at 440 nm) and lamp elevations for all participating instruments that reported results for both methods. The error bars indicate the standard deviations of the retrieved lamp and horizon elevations. Further, the result of a TLS fit and the 1:1 line are shown.